Fundamental research on the voltammetry of polycrystalline gold

Yang, S.

Citation

Yang, S. (2024, April 9). *Fundamental research on the voltammetry of polycrystalline gold*. Retrieved from https://hdl.handle.net/1887/3731809

一个简单误判引发的蝴蝶效应。

The butterfly effect triggered by a simple misjudgment.

I

Supporting Information for Chapter 2

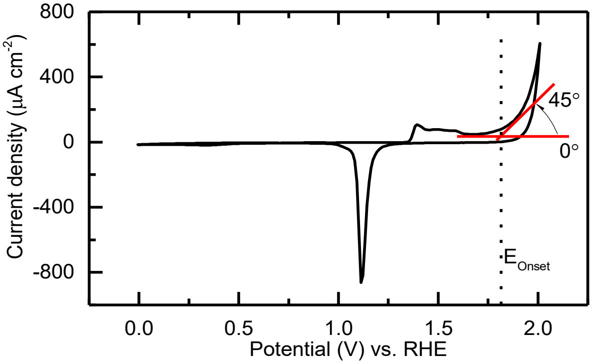

Fig. S1 The onset potential of OER is acquired by intersection of tangents between the baseline (horizontal line) and the rising current in the positive scan of cyclic voltammograms.[1] The angle between two intersection was fixed at 45°.

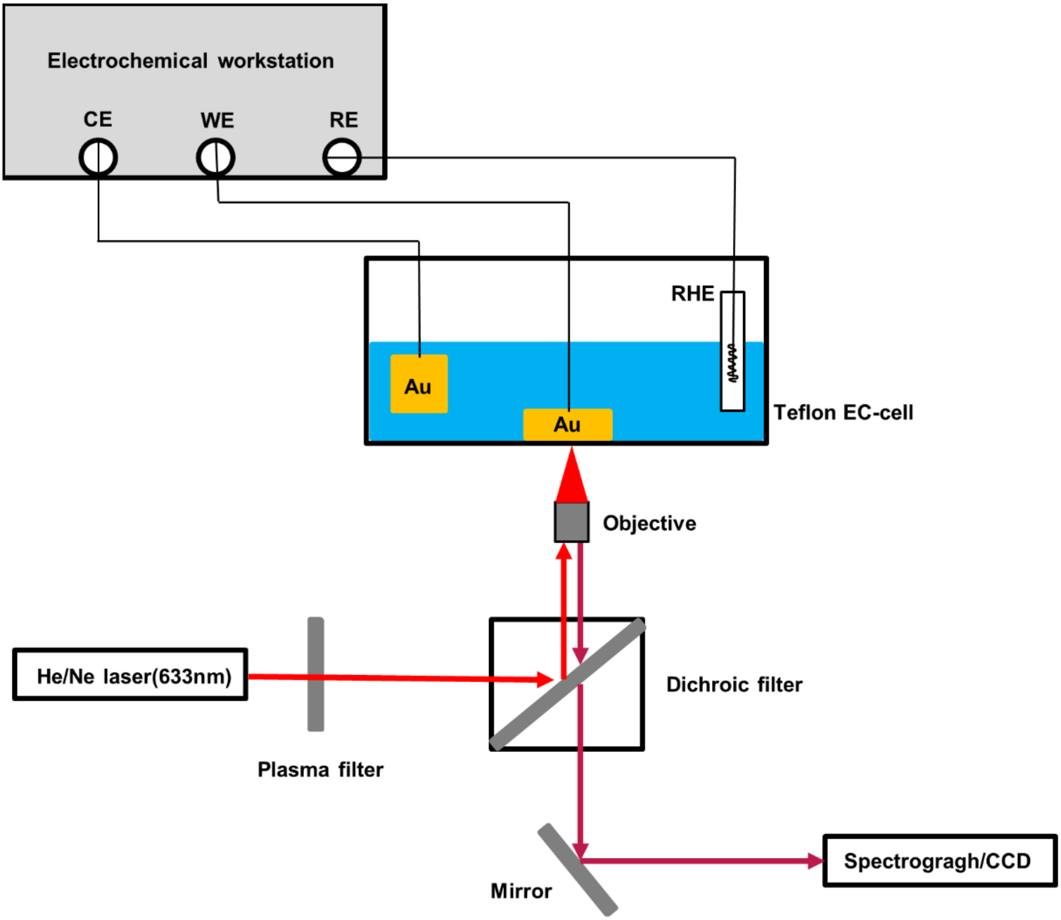

Fig. S2 Schematic diagram of electrochemical setup for in situ surface-enhanced Raman spectroscopic measurements.

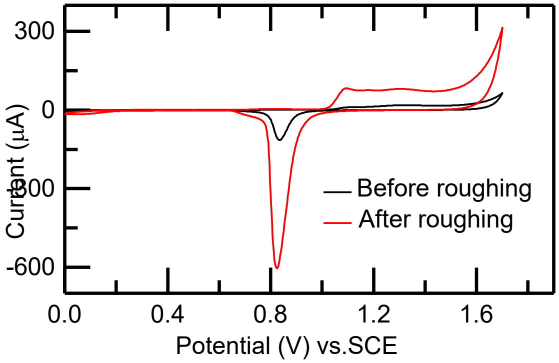

Fig. S3 Cyclic voltammogram of gold electrode at 50 mV/s in 0.1 M H_2SO_4 before and after gold surface roughing process. A successful roughing should show a significant enhanced current (at least 5 times) in a CV of roughed gold.

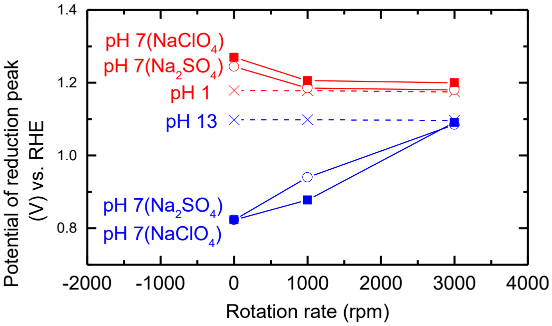

Fig. S4 The reduction potential where the α peak (red) and β peak (blue) are observed at different rotation rates. At pH 1 and pH 13 the positions of peak potential of the α and β peaks are not dependent on the rotation rate. At non rotating conditions the potential at which the α and β peaks occur has massively shifted in neutral solution compared to in the acidic and alkaline situation. However, upon rotation the potential of the α and β peak in neutral solution revert to the same position as observed in acidic and alkaline conditions. The peak potentials are obtained from Figure 3b in the main text.

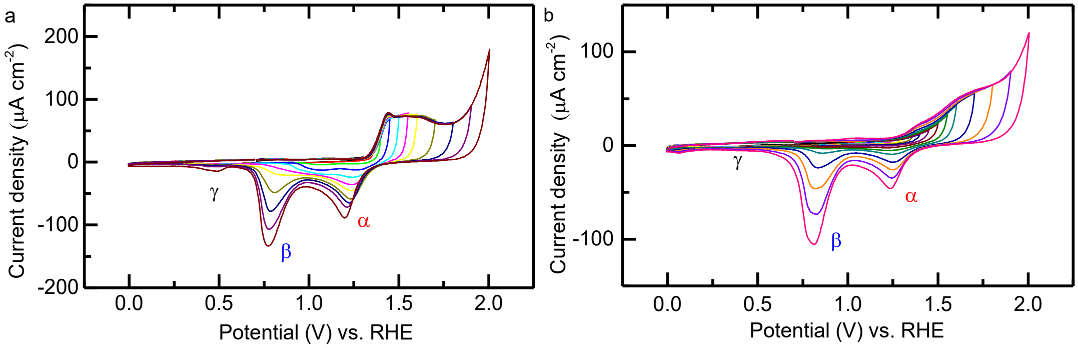

Figure S5 Cyclic voltammograms of gold at 50 mV/s with different upper potentials limits in (a) 0.1 M Na_2SO_4 or (b) 0.1 M $NaClO_4$.

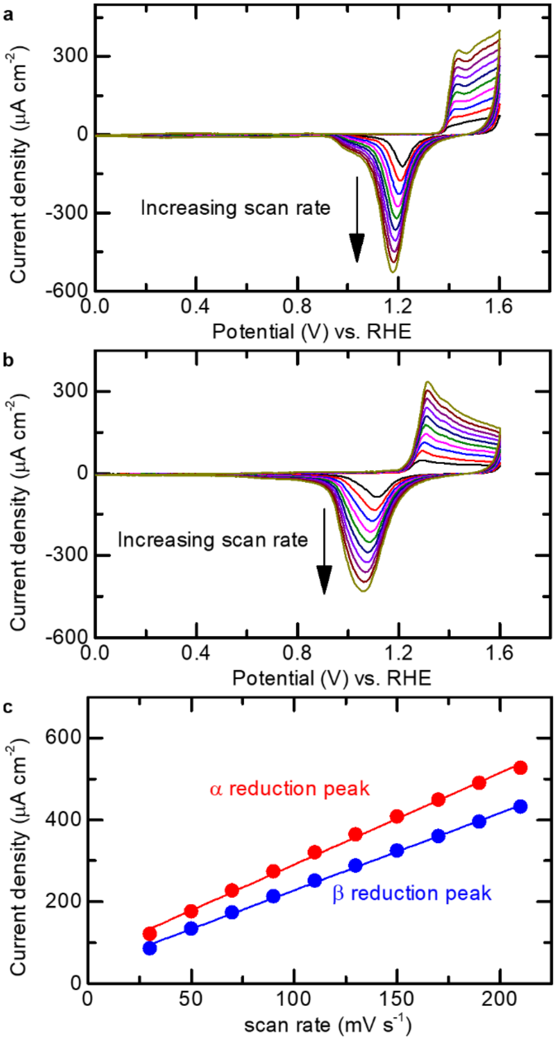

Fig. S6 CVs of gold at a range of scan rates between 30 and 210 mV/s in 0.1 M H_2SO_4 (a) or 0.1 M NaOH (b).Plot of peak currents of two oxides reduction as a function of scan rate.

Figure S6 shows the effect of scan rates to oxide reduction peaks. Because oxide reduction is an irreversible electrochemical process, both of two oxides show minor negative potential shift with increase of scan rate from 30 to 210 mV/s, as shown in Fig. S6, where α peak potential is at 1.16 ± 0.02 V and β peak potential is at 1.03 ± 0.03 V. Besides, reduction peaks was found to be linearly dependent on scan rates, not the square root of the scan rate. This reveals the redox reaction is confined to the electrode surface, i.e. no diffusion mode, which meet the characteristics of oxide reduction on the gold surface.

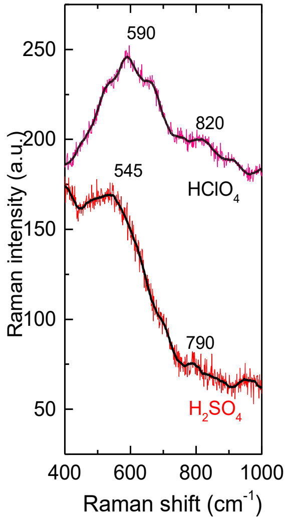

Fig. S7 In situ SERS of gold at 1.6V vs. RHE in Ar-saturated 0.1 M $HClO_4$ (pink line) and H_2SO_4 (red line) solution.. The ν(Au-O) vibration was observed at 590 cm^{-1} and the ν(O-O) vibration of Au-OOH was observed at 820 cm^{-1} in 0.1 M $HClO_4$ solution, which is consistent with previous reports in $HClO_4$ solution.[2-4] The ν(Au-O) vibration and the ν(O-O) vibration of Au-OOH have shifted to 545 cm^{-1} and 790 cm^{-1} in 0.1 M H_2SO_4 , which may be caused by adsorption of sulfate ions in H_2SO_4. Note that the ν(Au-O) vibration was reported to shift as a function of the oxidation potential.[4]

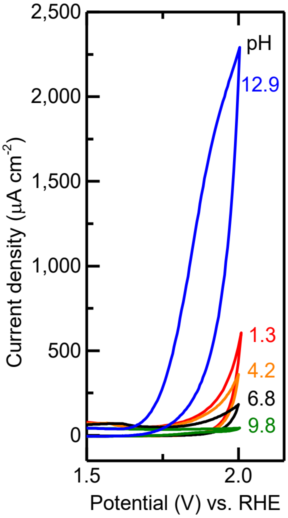

Fig. S8 Shown is the part of the CVs involving oxygen evolution, as a function of pH belonging to Figure 6a of the main text. Conditions: scan range is 0-2 V vs. RHE at 50 mv/s.

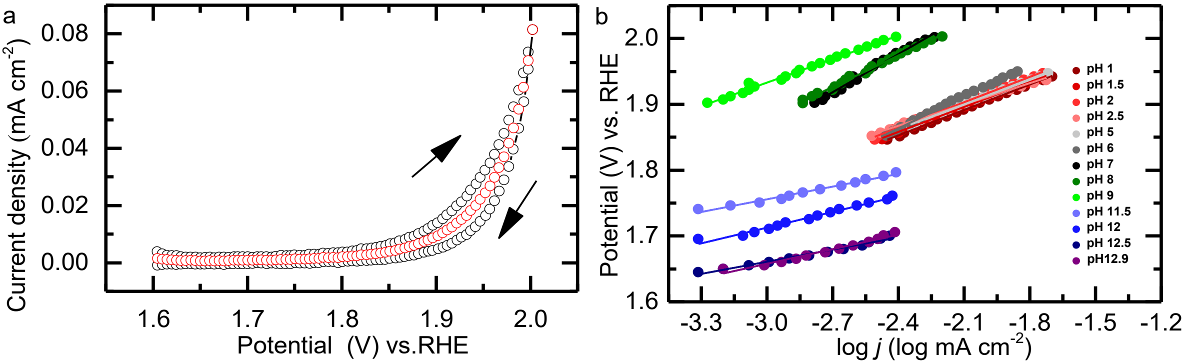

Fig. S9 a. OER activity was measured from the average (red) of the backwards (black) and forward (black) current density in a CV under steady-state conditions (1 mV s^{-1}). **b**. Tafel plot, which was obtained from the average of OER activity (red dot line in (a))

Table S1 Tafel slopes in different pH solution, which is calculated from Figure S9

pH	1	1.5	2	2.5	5	6	7	8	9	11.5	12	12.5	12.9
Tafel slope (mV/decade)	128	126	128	108	124	160	192	158	119	79	64	61	73

References

(1) Huang, Z. F.; Wang, J.; Peng, Y.; Jung, C.-Y.; Fisher, A.; Wang, X., *Adv. Energy Mater*. **2017**, *7*, 1700544.
(2) Liu, K.; Chen, T.; He, S.; Robbins, J. P.; Podkolzin, S. G.; Tian, F., *Angew. Chem. Int. Ed. Engl.* **2017**, *56*, 12952-12957.
(3) Diaz-Morales, O.; Calle-Vallejo, F.; de Munck, C.; Koper, M. T. M., *Chem. Sci.* **2013**, *4*, 2334-2343.
(4) Yeo, B. S.; Klaus, S. L.; Ross, P. N.; Mathies, R. A.; Bell, A. T., *Chemphyschem* **2010**, *11*, 1854-7

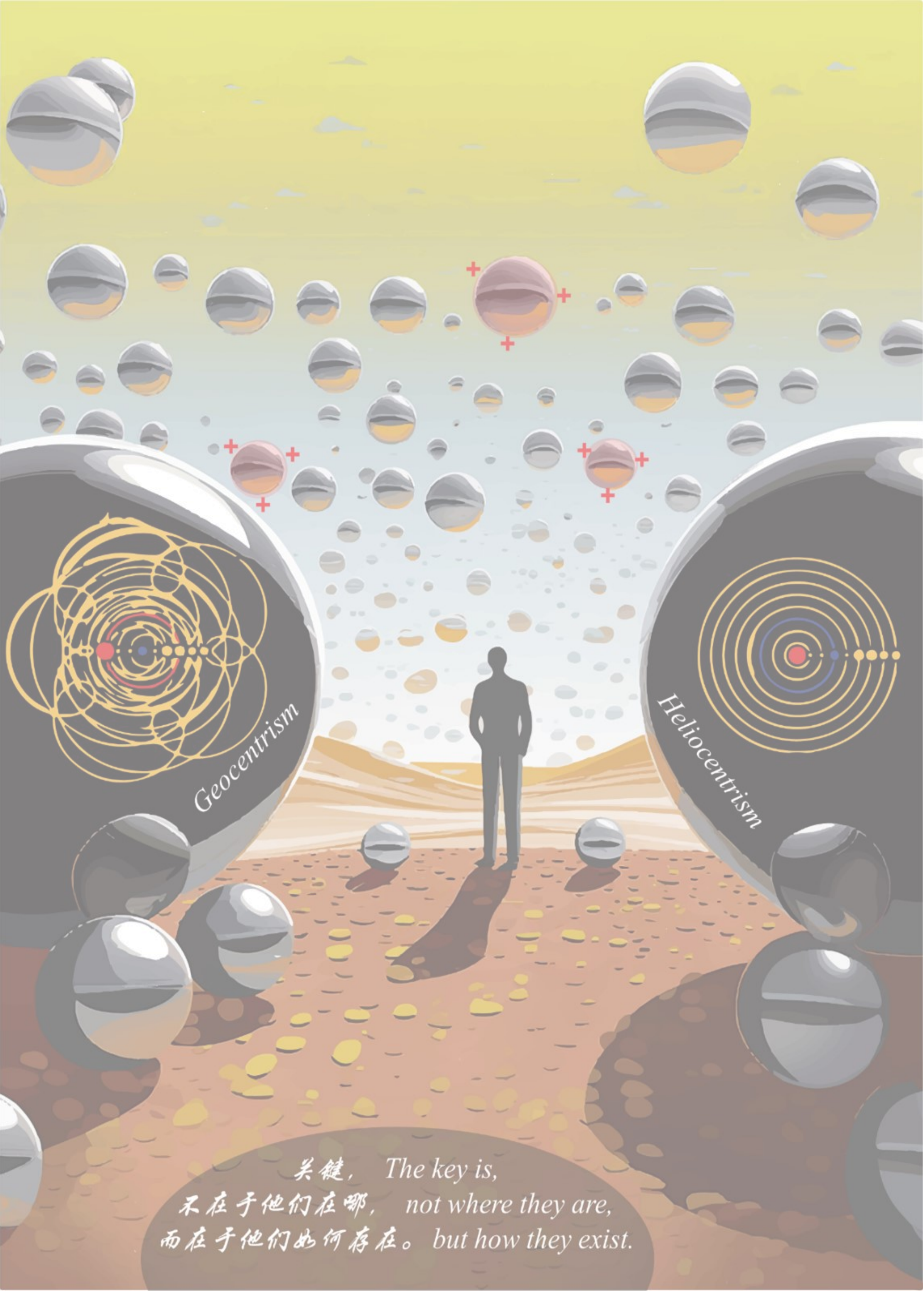
Geocentrism
Heliocentrism
关键， The key is,
不在于他们在哪， not where they are,
而在于他们如何存在。 but how they exist.

II

Supporting Information for Chapter 3

The PDF file includes:

- Materials and Methods
- Supplementary Text
- Figs. S1 to S16
- Tables S1

Materials and Methods

General.

All glassware was thoroughly cleaned to remove impurities by overnight submersion in an aqueous 0.5 M H_2SO_4 solution mixed with 6.3 mM $KMnO_4$, followed by removal of excess $KMnO_4$ on the glassware in diluted H_2SO_4 and H_2O_2. The glassware was subsequently rinsed five times and boiled three times in Millipore MilliQ water (resistivity is 18.2 MΩ cm). Prior to each electrochemical experiment, the glassware was boiled once in MilliQ water. Alumina suspensions (1.0, 0.3, and 0.05 μm) were obtained from Buehler. Electrolyte solutions were prepared with Suprapur® (Merck) reagents and MilliQ water. Determination of the pH was done using a Hanna Instruments HI 4222 pH meter which was calibrated using IUPAC standard buffers.

Electrochemical measurements.

All electrochemical measurements were conducted with Autolab PGSTAT 12, 204 and 128N potentiostats in combination with Autolab NOVA software and carried out in conventional single compartment three–electrode glass cells at around 25 °C. A PEEK encapsulated gold electrode ($A = 0.0314\ cm^2$, Metrohm) was used as working electrode, and a gold wire was the counter electrode, while a reversible hydrogen electrode (RHE) was employed as the reference electrode. Before a measurement, the working electrode (the PEEK encapsulated gold) was manually polished for 2 minutes with 1.0, 0.3, and then 0.05 μm alumina suspensions on Buehler cloth polishing pads, followed by sonication in MilliQ water for 10 minutes. A gold wire to be used as the counter electrode was flame annealed and rinsed with MilliQ water. The reference electrode (RHE) consisted of a Pt wire and was connected via a Luggin capillary and continuously bubbled with H_2 gas during each measurement.

The pH 1–13 solutions were obtained by mixing 0.1 M $HClO_4$, NaOH and $NaClO_4$. Unless stated otherwise, pH 1–13 represent solutions with fixed pH value comprising $HClO_4$, NaOH and $NaClO_4$ in this article and the ionic strength of the electrolyte solution was kept at 0.1 M. The solutions with different cations (Li^+, Na^+, K^+, Cs^+) and at different pH were obtained by mixing $HClO_4$, hydroxide and perchlorate salts, shown in fig. S3. Here, in order to better compare the effects of cations to gold oxide reduction, the concentration of electrolyte solution was kept at 0.05 M rather than 0.1 M due to the low solubility of $CsClO_4$. Dissolved oxygen was removed from the solution prior to each measurements by bubbling argon (purity grade 5.0) for at least 30 min. Argon was kept flowing above the solution during all experiments.

Rotating ring–disk electrode (RRDE)

RRDE experiments were conducted using an Autolab PGSTAT 12 potentiostat and a Pine Instruments MSR rotator. All measurements were done in a custom–build glass two–compartment cell with a three–electrode setup. A gold wire was used as a counter electrode, separated from the main compartment by a glass frit. A gold disk (A=0.196 cm^2) was used in conjunction with gold ring in a Pine Instruments E6R1 ChangeDisk setup. To detect the release of Au^{3+} from the disk, the ring was set at a fixed value below the potential of oxide reduction, and higher than the onset potential of the oxygen reduction reaction (E_{ORR}) on gold. Because E_{ORR} on gold changes with pH, the E_{ring} was set at 0.6 V in 0.1 M $HClO_4$ and $NaClO_4$ and at 0.9 V in an alkaline solution.

Electrochemical quartz crystal microbalance (EQCM)

The EQCM experiments were conducted using an Autolab PGSTAT 128N potentiostat and a 5 mL Autolab EQCM cell. An Autolab gold coated quartz crystal EQCM electrode (A = 0.35 cm^2, gold layer thickness = 100 nm) was used as the working electrode and a coiled gold wire was used as the counter electrode. An RHE Luggin setup was used as the reference electrode.(*37*)

Supplementary Text

S1. Literature overview of oxide formation

In general, the oxidation of noble metals includes the two–dimensional surface processes wherein OH and O chemisorption occurs, quasi–three dimensional surface reconstruction by a place exchange between the OH and/or O species and surface metal atoms, and thickening of the oxide film in a high electrostatic field or upon long oxidation times. Historically, cathodic reduction of oxide was mainly used to determinate the oxide thickness and to investigate the different layers of oxides. For the reduction of a metal oxide ($M_2O_x + 2xH^+ + 2xe^- \rightarrow 2M + xH_2O$), the Nernst equation indicates that the reduction potential of oxide should not change on the RHE scale. However, such metal oxide reduction peaks often do show an abnormal potential shift. i.e. a non–Nernstian shift, especially when the oxidation potential increases. It is worth noting that non–Nernstian behavior is not only observed for noble metal oxides but has been extensively reported in case of many other metal oxides.(*7, 38-40*)

Explanations of the non–Nernstian behavior of the reduction of metal oxides vary substantially over literature, such as the strong effects of anions chemisorption, (*41*) a hysteresis behavior caused by the irreversible quasi–3 dimensional oxide formation(*11*), the effect of oxidation state changes, (*42, 43*) or a slow reduction process of the outer layer of a thick oxide (*21, 24*). We must point out that these above discussions are speculations and were never directly proven leading to a rather one–sided conclusion.

Non–Nernstian behavior of metal oxide reduction reactions often appear in oxide corrosion studies.(*26, 44*) This triggered the hypothesis whether the non–Nernstian behavior of the oxide reduction reaction may be directly caused by the self–reconstruction of oxides. Gold is frequently seen as the most ideal noble metal for the investigation of oxide formation. First, gold has very weak chemisorption properties so that it shows a wide double layer region, thereby avoiding the effect of co–adsorption of electrolytes during the oxide reduction process. Second, Au(+III) has been shown to be the only stable oxidation state observed in gold oxides by ex situ X–ray photoelectron spectroscopy(*22*) and in situ extended X–ray absorption fine–structure studies.(*23*) Normally only two stable forms of oxidized gold can be observed in the Pourbaix diagrams of gold, i.e. auric oxide (Au_2O_3) and gold trihydroxide ($Au(OH)_3$),(*44*) as shown in fig. S9.

In our previous research, we found that two independent forms of gold oxides, i.e α and β, are present at all pH values when the initial oxide layer forms.(*8*) The α phase is preferably formed in an acidic environment, while the β phase is preferably produced under alkaline conditions. Both phases can coexist in neutral solutions. We assigned the two oxides to Au_2O_3 (α oxide) and $Au(OH)_3$ (β oxide) by combining our in situ Surface–Enhanced Raman Spectroscopy (SERS) experiment and computational results by the Koper group.(*45*) However, all these previous studies do not answer why the oxide reduction peaks show non–Nernstian behavior.

S2 Detection of hydration shells surrounding Au^{3+} at neutral conditions by the RRDE ring

In the RRDE experiment at pH 7, when the potential is negatively scanned in order to reduce gold oxide, the consumed protons in the β oxide reduction reaction most likely do not stem from the bulk solution, but must come from the hydration shells of Au^{3+} itself. Consumed protons are not easily compensated for given that the concentration of protons at neutral conditions is low. Therefore the pH of the surface hydration shells must increase rapidly, especially at pH 7. This causes the hydration shells to obtain a negative charge at its surface:

$$Au(OH)_3 \cdots (H_2O)_n Au^{3+} + 3e^- \rightarrow Au + 3H_2O + (HO^-)_3(H_2O)_{n-3}\,Au^{3+}$$

Based on the Nernst-Planck equation, the total current distribution is a summation of a diffusion, convection and migration in a RRDE experiment.(*27, 28, 46, 47*) The ionic migration is driven by the gradient of electric filed ($\Delta E/l$) in the potential (ΔE)) over distance (l).(*27*) In the presence of an excess of supporting electrolyte, the ionic migration to the flux of electroactive species is often neglected to simplify the mass transfer conditions. (*47*) However, for many cases $\Delta E/l$ is hard to reduce and the ionic migration affect remains important in a RRDE experiment.(*28, 46*)

In RRDE experiments in a neutral solution, we observed that a positive current appears first on the ring, and is followed by a negative current ,when E_{ring} is set at higher than 0 V vs. RHE (fig. S4). Our observations are as follows:

1) The positive current is observed first and is followed by a negative current. This is independently of the lower vertex potential and scan direction set at the disk (fig. S4A-D).

2) The positive current is heavily dependent on the rotation rate (fig. S4E-F), and largely disappears at high mass transport rates (fig. S4F).

3) When change the rotation rates, the negative current detected on the ring does not change, while the positive current rapidly decreases with increasing rotation rates. While the positive current decreases, the potential at which the negative current occurs starts to shift to more positive potentials (fig. S4E).

4) Additionally, the positive current can be detected at low E_{ring} (E_{ring}> 0 V vs.RHE), which excludes the formation of most reactive oxygen species being responsible.

This reflects that the observed delay of Au^{3+} reduction is directly related by an event that apparently causes an unusual positive current on the ring. Based on these observation, we deduced that the positive current does not belong to a Faradaic current caused by an oxidation reaction, but should be assigned to a non-Faradaic current that is caused by the migration of considerably large hydration shells that accompany Au^{3+}, and largely have a negative charge due to the gold oxide reduction reaction mediated under neutral conditions. When the rotation rate increases the mass transfer of proton, the electronegativity decrease as the hydration shell is refreshed.

These hydration shells with a negatively charged surface migrate to the ring of RRDE to initially cause a non–Faradaic positive current, as shown in fig. S4. Detection of such a non–Faradaic positive current is therefore considered as a significant finger print for the presence Au^{3+} bearing a significant hydration shells at the surface of gold oxide. There are two ways to reduce the Au^{3+} cations present within these hydration shells:

1) A step–by–step reduction including shell release, shell peeling and finally Au^{3+} reduction. This process shows a delayed Au^{3+} reduction current on the ring due to an interference with the non–Faradaic caused by the shell migration and due the slow shell peeling process (fig. S4).

2) A direct reduction of Au^{3+} can be performed at a sufficiently negative ring potential (< 0 V) that is necessary to overcome the energy barrier for electron tunneling through the hydration shells (Fig. 2D)

S3 The presence of ionized Au^{3+} and hydrous Au^{3+} on the oxides surface relates to the stability of the interface double layer

Our EQCM results show that the mass loss does not start at the beginning of the oxide reduction process. Instead the mass loss takes place immediately and quickly when the potential is scanned over a particular threshold value (E_ψ). In an acidic solution (Fig. 3B), when E_+ is set below 1.5 V, the emergence of E_ψ is independent of E_α and E_β. Yet E_ψ shifts consistently with E_α once $E_+ > 1.5$ V. Our RRDE experiments show that ionized Au^{3+} exists in α oxide when $E_+ > 1.5$ V.(Fig. 2B) This suggests that the presence of Au^{3+} relates to the behavior of E_ψ as well.

It is important to note that the detected frequency changes reflect the mass change of the absorption layer, which does not only include the actual oxide layer itself, but also the rigid adsorption layer at the solid-electrolyte interface, which relates to the interface properties (viscosity, density etc.) and weight of the solvation shell and ions present therein. (*30-32*) In fig. S8, we compared the difference between the oxide mass change calculated from the overall charge transferred during the gold oxide formation, and the total mass change detected by the QCM. In an acidic solution, when ionic Au^{3+} forms on α oxide (E_+>1.5V), total mass increase is always bigger than the gold mass increase, as shown in fig. S8A. A similar phenomenon also happens in a neutral solution (fig. S8C), when hydrous Au^{3+} forms on β oxide (E_+>1.5V). Those observations clearly show that ionized Au^{3+} and hydrous Au^{3+} have the ability to fix more molecules resulting in a heavier double layer, as shown in Fig. S8B and

D. It worth to note that the extra mass change caused by hydrous Au^{3+} is much bigger than that caused by ionic Au^{3+}. This indicates hydrous Au^{3+} ions bound to β oxide has a stronger ability to bind molecule tightly in a neutral solution than ionic Au^{3+} ions bound on α oxide in an acidic solution. No significant additional mass is detected by EQCM if no Au^{3+} is present at the electrode surface. Under those conditions the mass changes detected by the EQCM fit well with the presence of the lattice oxygen atoms belonging to the stoichiometry of Au_2O_3 and $Au(OH)_3$.

According to our EQCM and RRDE experiments, the reduction of α oxide and the release of Au^{3+} start at the same time, i.e. the onset potentials of α reduction and Au^{3+} release are the same as observed by RRDE experiments (fig. S11A). However, the mass loss starts only when the scanning potential approaches E_α (fig. S5B). The change of E_ψ also follows a similar trend in neutral and alkaline solutions: E_ψ is always closer to the peak potential rather than the onset of the reduction reaction. Based on past research, oxide reduction is expected to occur via a bottom-to-top reduction process on the oxide surface.(*11*) This indicates that the bottom part of oxide should be reduced first when scanning the reduction potential over the onset potential of an oxide reduction peak. And the top part of oxide may not be reduced until the scanning potential approaches the peak potential. Therefore we deduce that the emergence of E_ψ is most likely related to the presence of Au^{3+} at the outer surface of the oxide layer. The stable structure of the double layer in the oxide–electrolyte interface will be broken due to the disappearance of Au^{3+} at the oxide surface upon reduction.

Tracing correlations between E_ψ, E_α and E_β during a CV experiment allows one to understand the role of Au^{3+}at the surface in relation to the stability of the gold oxide structure. In a neutral solution (Fig. 3C and fig. S6), when $E_+ < 1.9$ V, the existence of ionized Au^{3+} in α oxide and hydrous Au^{3+} in β oxide can be recognized on the basis of their non–Nernstian behavior at the same time. However, the EQCM data shows that E_ψ only relates to E_β and not to E_α, indicating that only hydrous Au^{3+} at β oxide are present on the surface under these conditions (fig. S6A). When E_+ is set in the range of 1.9–2.1V, the existence of two separated E_ψ values indicates that both ionized Au^{3+} at α oxide and hydrous Au^{3+} at β oxide are present on the surface (fig. S6B-D). When E_+ is set above 2.1 V, the effect of hydrous Au^{3+} to stabilize the interface disappears (fig. S6E-F). At these conditions H_2O molecules from the hydration shells are oxidized to O_2. Unless hydration of the Au^{3+} sites is sufficiently rapid compared to the evolution of dioxygen, only ionized Au^{3+} will remain on the oxide surface.

S4 Identification of Au^{3+} saturation at the oxide surface by EQCM

As described in section S3, the E_ψ observed by EQCM experiments is a powerful indicator to reveal the presence of Au^{3+} ions at the surface of the gold oxide layer. In an acidic solution (Fig. 3B), when Au^{3+} is bound to α oxide ($E_+ > 1.5$ V), E_ψ and E_α show a consistent non–Nernstian behavior with the increase of E_+. However the consistency between E_ψ and E_α is broken when $E_+ > 2.1$ V. Here E_ψ and E_α separate upon further increase of E_+. The separation between E_ψ and E_α also appears in neutral solutions once $E_+ > 2.1$ V (Fig. 3C). Although the amount of Au^{3+} increases with E_+, there must be a maximum value for the amount of Au^{3+} that can realistically bind to the oxide surface due to the limited amount of binding sites. Further increasing E_+ will cause more Au^{3+} to be formed. Due to a lack of sufficient binding sites on the Au_2O_3 surface, these Au^{3+} ions will escape from the rigid interface into the diffusion layer.

For Au^{3+} ions binding to the oxide surface, their reduction reaction proceeds simultaneously with reduction of the oxide layer. This is illustrated by the non-Nernstian negative shift of E_α, when the amount of Au^{3+} at the surface increases. Yet, for free Au^{3+} species that have diffused into the solution, its reduction can only occur once the gold oxide layer has largely been reduced. Although free Au^{3+} produced upon the oxidation of gold shows a reversible reduction wave at a very high scan rate at an early stage of the oxide formation (fig. S10A), reduction of free Au^{3+} becomes fully irreversible when a thick oxide layer is formed. Apparently, reduction of free Au^{3+} is fully blocked by the oxide layer.

The actual reduction of free Au^{3+} occurs negatively from E_α due to Au^{3+} mass transport processes from the solution to the electrode.(*48*). Given that E_α and the reduction of free Au^{3+} are not deconvoluted, the E_α peak shifts more negatively, while E_ψ does not. After all reduction of free Au^{3+} occurring in solution is not picked up by the microbalance.

The saturation of the gold oxide layer with ionic Au^{3+} hardly appears in case of β oxide in alkaline solutions, even when very high oxidation potentials are applied. This is due to regeneration of $Au(OH)_3$ upon hydroxylation of Au^{3+} as soon as it is formed. This also explains well why E_ψ and E_β shift consistently under these conditions even at a high oxidation potentials. (Fig. 3D).

S5 Calculating the amount of Au^{3+} in α oxide based on the slope in the E_α– pH plot

When E_+ is set to higher values, Au^{3+} is formed at the oxide surface and will bind to the exposed oxide sites of α oxide (Au_2O_3) via ionic interactions. The structure of α oxide therefore must change from a fully covalent oxide (Au_2O_3) to a covalent–ionic oxide ($Au_2O_3 \cdots xAu^{3+}$), where x represents the amount of Au^{3+} per α oxide site. According to our EQCM analysis, E_ψ and E_α show a simultaneously negative shift upon an increase of E_+ when E_+ is set at or above 2.1 V. This is the result of more ionized Au^{3+} stabilizing Au_2O_3 through the formation of ionic bonds. However, when E_+ is set above 2.1 V, E_ψ and E_α will separate, indicating that ionized Au^{3+} has become saturated at the α oxide layer and free Au^{3+} migrates into the diffusion layer (see section S4). Here, we have defined that y represents the number of free Au^{3+} equivalents in solution.

When $E_+ < 2.2$ V vs. RHE, y=0 as we do not observe any separation between E_ψ and E_α in our EQCM experiments, indicating that no free Au^{3+} has formed yet. Under these conditions the α oxide reduction reaction can be expressed as

$$Au_2O_3 \cdots xAu^{3+} + 6H^+ + 3(2+x)e^- = (2+x)Au + 3H_2O \text{ (1)}$$

Its Nernst equation should then be formulated as:

$$\Delta E_\alpha = -0.059\left(\frac{2}{x+2}\right) \times \text{pH (2)}$$

which indicates that E_α will change as a function of the pH on the RHE scale given that $\frac{2}{x+2} \neq 1$. This allows us to trace the amount of α oxide–$Au_2O_3 \cdots xAu^{3+}$ formed on the basis of the slope of $K = 0.059(\frac{x}{x+2})$ (vs. RHE) (see fig. S15). Indeed we observed that the slope of

E_α vs pH increases with E_+.(Fig. 1B) The relation between x and E_+ is shown in table S1. The amount of Au^{3+} per α oxide site increases from 0 to 0.4 before the oxygen evolution reaction (OER) commences and eventually reaches a value of 0.9 during the OER process at 2.1 V vs. RHE.

An assumption that we make here is that x does not further increase after the oxide layer has become fully saturated with Au^{3+} when $E_+ \geq 2.2$ V vs. RHE. In other words we expect $x \leq 1$, given that there are only a limited amount of sites on the surface of α oxide. It is indeed at $E_+ \geq 2.2$ V vs. RHE, where separation between E_ψ and E_α can be observed (Fig. 3 B, C). This suggests that Au^{3+} first binds to the surface of α oxide, and once the surface is fully saturated, it is lost to the double layer as free Au^{3+}.

The K value does show a slow increase below E_{OER} but rapidly increases at potentials above E_{OER} during a standard cyclic voltammetry experiment(see Fig. S15). This indicates that large amount of Au^{3+} forms at potentials above E_{OER}. It is worth noting that the increasing trend of Au^{3+} has also been directly observed in a previous metal corrosion study by a setup composed of a micro–electrochemical scanning flow cells (SFC) and inductively coupled plasma mass spectrometer (ICP–MS), where Cherevko *et. al*. found that the amount of gold cations detected is relatively minor at potentials below the onset for OER but quickly increase when the oxygen evolution reaction commences.(*26*)

S6 Transformations between ionized Au^{3+} and hydrous Au^{3+}

The complexity of the liquid–solid interface at neutral conditions is caused by the presence of both ionized Au^{3+} and hydrous Au^{3+}, and which cause different non–Nernstian shifts. Yet by carefully examining the presence of the α and β oxide peaks and their non–Nernstian shifts we can pinpoint how the oxide surface structure changes as a function of the applied reaction conditions.

First, there must be a competition between ionized Au^{3+} and hydrous Au^{3+} illustrated in fig. S12, which is dependent on the nucleophilicity of H_2O at the operating pH, and the nucleophilicity of the oxygen sites of the metal oxide surface. When the pH is closer to 4, H^+ will inhibit the nucleophilicity of H_2O resulting in ionized Au^{3+} being formed preferably over hydrous Au^{3+}. However, when the pH is closer to 7, the formation of hydrous Au^{3+} will prevail over ionized Au^{3+}. The importance of the nucleophilicity of H_2O for the Au^{3+} hydration shell formation is shown in fig. S16. If we oxidize gold at a high oxidation potential and then directly scan in a negative direction without any stirring, the α reduction peak occurs at 1.29 V (red line in fig. S16). However, if we use MilliQ–water to rinse the oxidized gold electrode first and place the oxidized gold into a fresh 0.1 M $NaClO_4$ solution to measure a CV, we can see a significant shift with more than –0.6 V, which points to a transition from α oxide to β oxide. Furthermore, the β peaks shows a more negative shift if we increase the oxidation time to produce more Au^{3+} (see blue, purple and dark blue line in fig. S16). This illustrates that ionized Au^{3+} reduced at 1.29 V turns into hydrous Au^{3+} reduced below 0.7 V after rinsing with MilliQ–water ($\cdots Au^{3+} \xrightarrow{nH_20} \cdots (H_20)_n Au^{3+}$), as shown in the insert of fig. S16. It worth noting that the hydrous β oxide formed by MilliQ–water rinsing shows a significant more negative shift than the samples produced in 0.1 M electrolyte. This indicates that a more stable hydrous oxide is formed in MilliQ–water compared to water that is devoid of any electrolyte.

The non–covalent interactions of Au^{3+} with the oxide surface must be weak, independent whether these are ionic interactions at acidic conditions, or hydrogen bond interactions at neutral conditions. This means we can manipulate the levels of both ionized Au^{3+} and hydrous Au^{3+} by changing the rotation rate. Both the α and β peaks can still be observed when rotation rates are set below 400 rpm (see lower part in fig. S4A). Interestingly, the non–Nernstian behavior of the α and β peaks disappears when fast rotation rates are set (3000 rpm). In this latter experiment the ionized Au^{3+} and hydrous Au^{3+} species apparently dissociate from the oxide surface and are lost to the bulk solution (see fig. S13A and fig. S14A). If we increase E_+ , the β peak still will show a gradual negative shift, even at 3000 rpm (see fig. S13B and fig. S14B). When E_+ is set above E_{OER}, the mutual transformation between the α peak with ionized Au^{3+} and the β peak with hydrous Au^{3+} can be observed during the OER process by changing the rotation rate from 0 rpm to 3000 rpm.(see fig. S13C and fig. S14C). At 0 rpm mostly α oxide is present in the cyclic voltammogram, while experiments at 3000 rpm mainly show the formation of β oxide. The water of the hydration shells is consumed during the OER process, and will lead to the transformation of hydrous Au^{3+} to ionized Au^{3+} at non rotating conditions (0 rpm) due to a local accumulation of H^+. Yet at a high rotation rate (3000 rpm) both the mass transport of water and protons are faster, allowing for the hydration shell structure to be refreshed timely. The mutual transformation between ionized Au^{3+} and hydrous Au^{3+} is independent of whether $NaClO_4$ or Na_2SO_4 is used as an electrolyte. (fig. S13 and fig. S14)

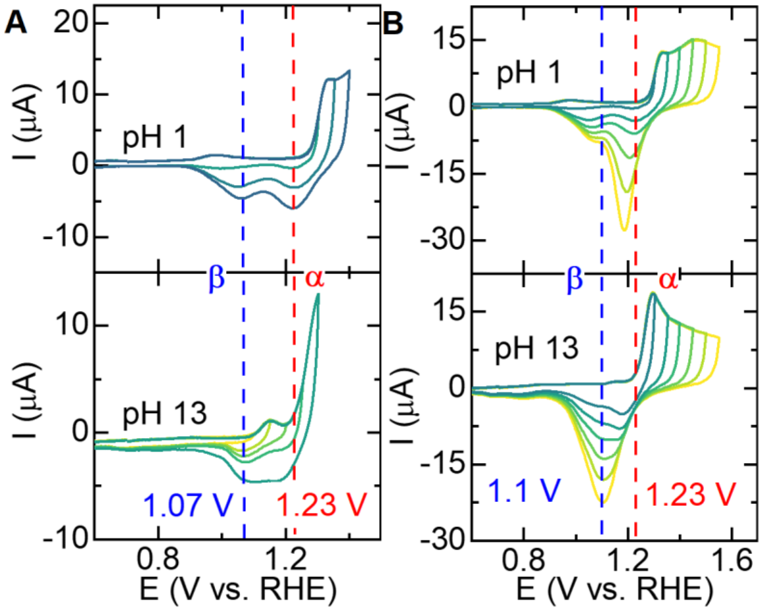

Fig. S1 Cyclic voltammograms of gold at 50 mV/s in pH 1 and 13. (**A**) E_+ was varied from 1.1–1.4 V; (**B**) E_+ was varied from 1.35–1.55 V; The red and blue dash lines represent the reduction peak potential of initial formation stage of α and β oxide, respectively.

When E+ is changed from 1.25 to 1.5, the β peak shows a minor +0.03 V shift from 1.07 to 1.1 V, which reflects the process from reversible adsorbed OH^- to a stable bulk–phase solid $Au(OH)_3$.(*8*) The minor shift of the β peak is independent of the pH, i.e. it follows Nernstian behavior. Because the values of 1.23 V for the α peak and 1.1 V for the β peak are constants providing that the potential (E_+) is kept low, they are used to represent the reduction potential non-shifted α and β oxide in our main text, respectively.

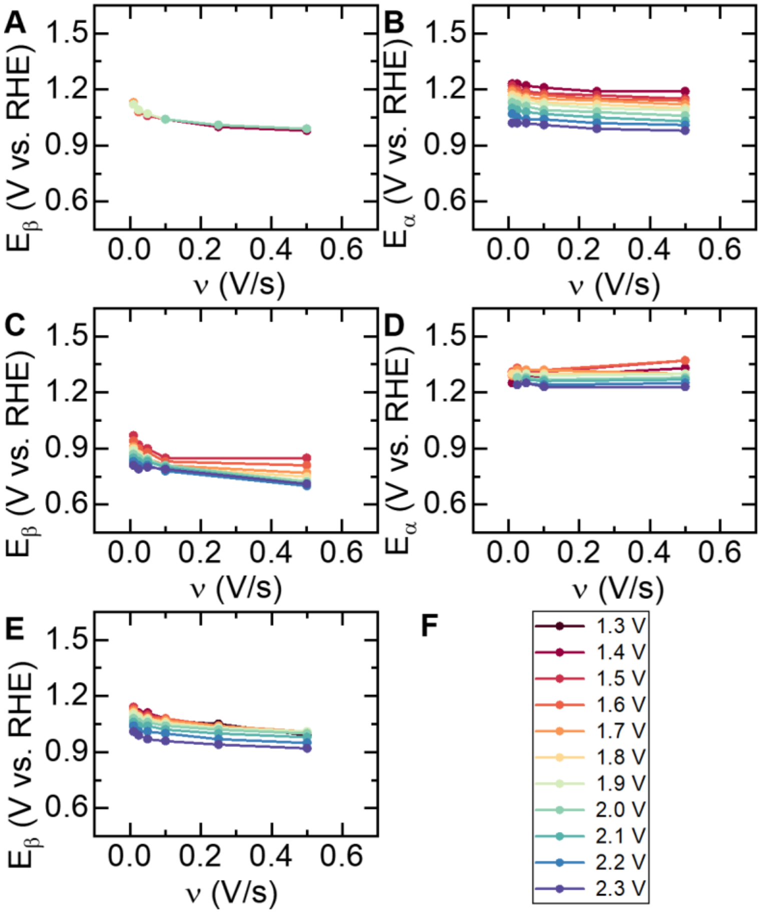

Fig. S2 The potential of the β (E_β) and α (E_α) reduction peaks with the increase of E_+ in the scan rate (ν) of 0.01-0.5 V/s in 0.1 M $HClO_4$ (**A-B**), $NaClO_4$ (**C-D**), NaOH (**E**). (**A**) E_β in 0.1 M $HClO_4$; (**B**) E_α in 0.1 M $HClO_4$; (**C**) E_β in 0.1 M $NaClO_4$; (**D**) E_α in 0.1 M $NaClO_4$; (**E**) E_β in 0.1 M NaOH; (**F**) different colorful lines shown in (**A-E**) represent the change of E_+ from 1.3V to 2.3 V on the RHE scale.

The appearance of the non–Nernstian behavior of the α and β peaks are largely consistent when the scan rate between 0.01 to 0.5 V/s, as shown in fig. S2. This indicates that the observed non–Nernstian behavior is not caused by kinetic effects. It also allows one to extrapolate the outcome to a scan rate of 0 V/s, thereby excluding any pH effects that may occur during the reduction of α and β oxide.

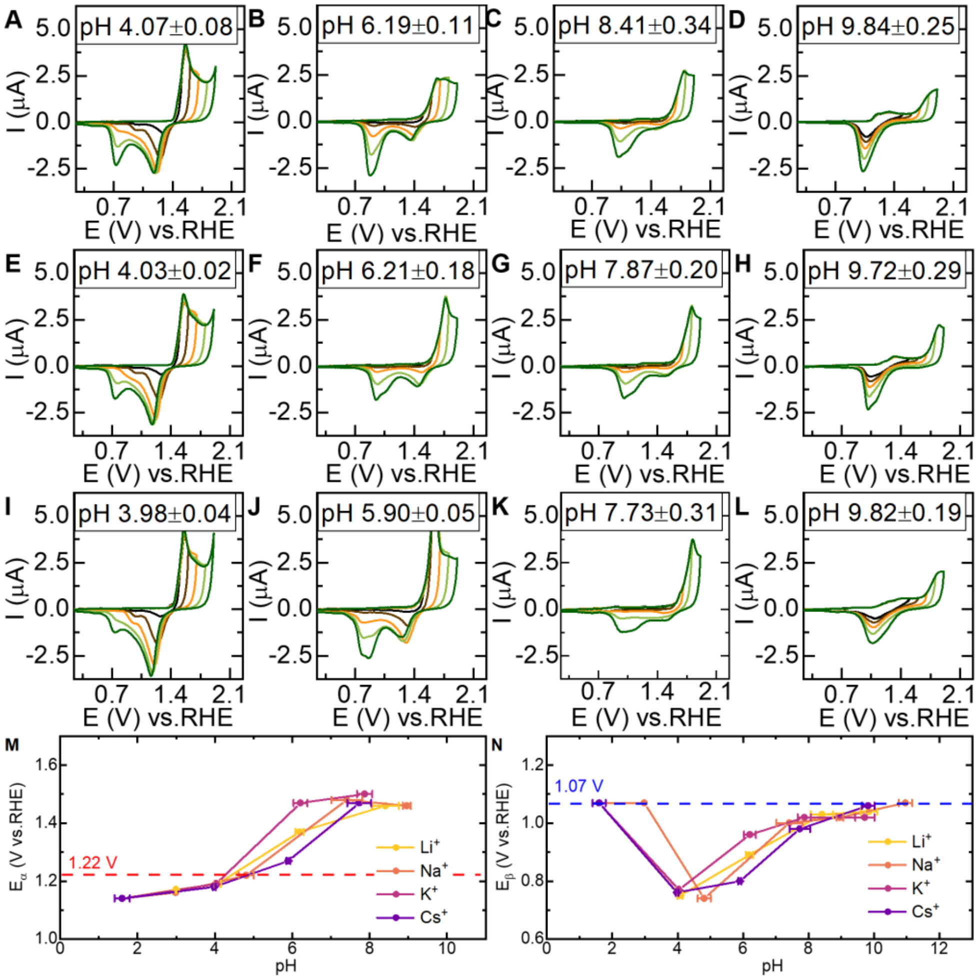

Fig. S3 Cyclic voltammograms of gold with varying E_+ in the range of 1.5–1.9 V at different pH in 0.05 M $LiClO_4$ (**A-D**), $KClO_4$ (**E-H**), $CsClO_4$ (**I-L**); (**M**) E_α of CVs (0-1.8 V vs. RHE) with changing solution pH at 0.05 M different cations and red dash line represents the reduction peak potential of initial formation stage of α oxide; (**N**) E_β of CVs (0-1.8 V vs. RHE) with changing solution pH at 0.05 M different cations and the blue dash line represent the reduction peak potential of initial formation stage of β oxide. The error represents the deviation of solution pH before and after measurements.

The non–Nernstian behavior of the β peak is most significant in neutral solutions, as shown in Fig. S3. The non–Nernstian shifts of the α and β peaks are highly consistent when we change anion (SO_4^{2-} and ClO_4^- shown in our previous work) (*8*) or the type of cation (Li^+,

Na^+, K^+, Cs^+ in Fig. S3) present in the electrolyte. We therefore can exclude electrolyte adsorption playing a major role here.

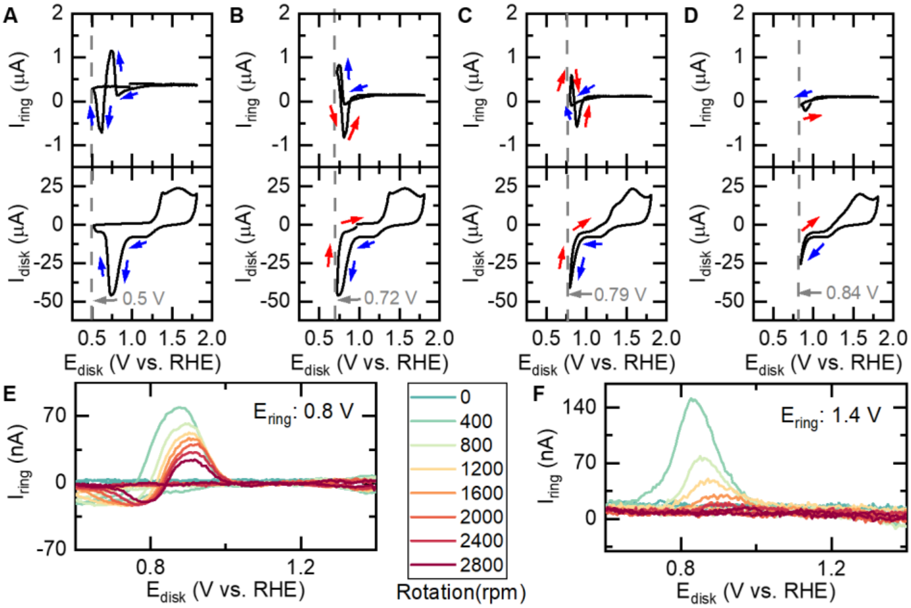

Fig. S4 (A–D) Rotating ring–disk electrode (RRDE) measurements of gold in 0.1 M $NaClO_4$ at 50 mV/s. E_{ring} is set at 0.6V, the rotation rate is 400 rpm. The blue arrow represents that the CV is negatively scanned. Red arrow represents that the CV is positively scanned. The grey dash line is to highlight E_- in a CV. The range of E_{disk}: **(A)** 0.5–1.8 V; (**B**) 0.72–1.8 V; (**C**) 0.79–1.8 V; (**D**) 0.84–1.8 V. **(E-F)** The change of I_{ring} with various rotation rates (rpm) in RRDE measurements of gold in 0.1 M $NaClO_4$ at 50 mV/s. E_{ring} is set at 0.8 V (**E**) and 1.4 V (F), respectively.

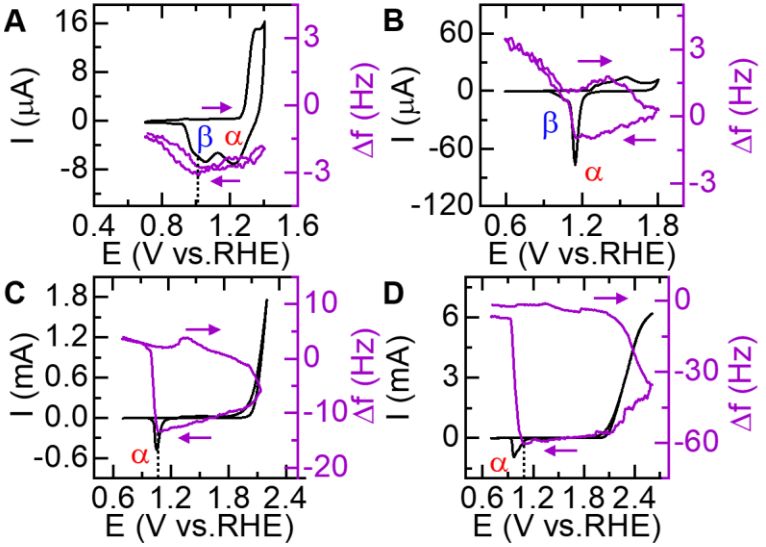

Fig. S5 Electrochemical quartz crystal microbalance measurement with a gold working electrode at 50 mV/s in 0.1 M $HClO_4$. The selected potential range is: **(A)** 0.7–1.4 V; **(B)** 0.7–1.8 V; **(C)** 0.7–2.2 V; **(D)** 0.7–2.6 V vs. RHE. The dash line shows the onset potential of mass loss (E_ψ) which reflects the potential in which the QCM signal starts to increase, i.e. mass loss, in the scanning process of a CV.

In EQCM experiments recorded in an acidic solution (Fig. 3B), the frequency change (Δf) was not observed only after the two oxides have been completely reduced, providing that E_+ is set below 1.5 V (fig. S5A)**.** When E_+ is set above 1.5 V, E_ψ immediately changes to the same potential as E_α and shifts negatively with E_α when E_+ is increased further (fig. S5B). The potential shift behavior of E_ψ will stop around 1.08 V while E_α continues to shift to more negative potentials when E_+ is set in the range of 2.1 to 2.6 V (fig. S5C–D).

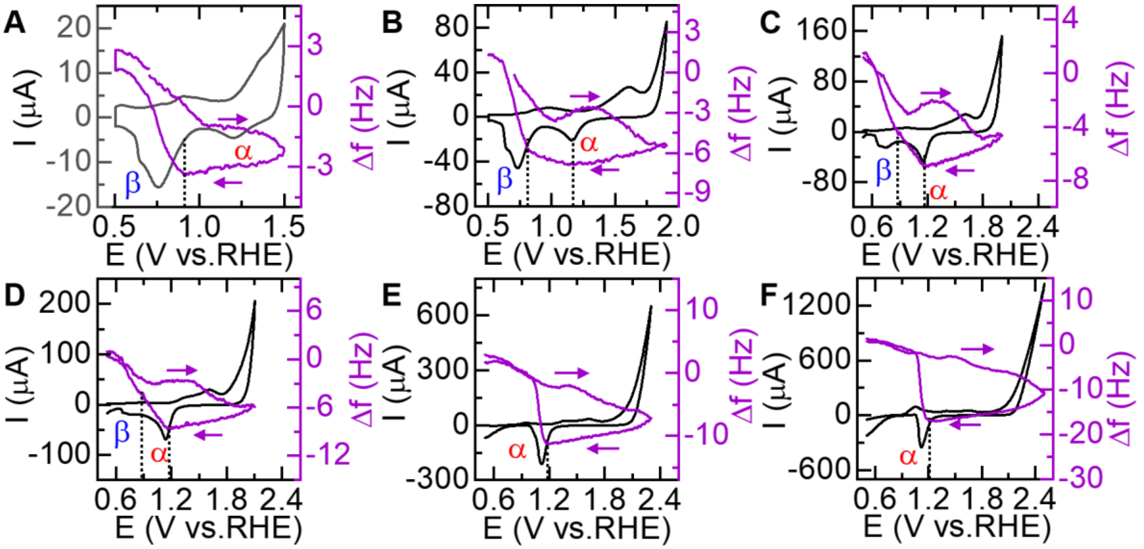

Fig. S6 Electrochemical quartz crystal microbalance measurement with a gold working electrode at 50 mV/s in 0.1 M $NaClO_4$. The potential range set is: **(A)** 0.7–1.5 V; **(B)** 0.7–1.9 V; **(C)** 0.7–2 V; **(D)** 0.7–2.1 V; **(E)** 0.7–2.3 V; **(F)** 0.7–2.5 V vs. RHE. The dash line shows the onset potential of mass loss (E_ψ) which reflect the potential in which the QCM signal starts to increase, i.e. mass loss, in the scanning process of a CV.

When the EQCM experiment is taken in a neutral solution (Fig. 3C), E_ψ appears in the first half of the β peak but shows no relationship with the α peak even though a shift of the α peak can be observed when E_+ is changed, yet kept below 1.9 V. Once E_+ is set to 1.9 V, E_ψ suddenly shifts to 1.16 V, which now coincides with E_α. From this point onwards, E_ψ and E_α shift consistently in the E_+ range of 1.9–2.1 V. Eventually E_ψ and E_α will separate gradually when E_+ is set above 2.1 V.

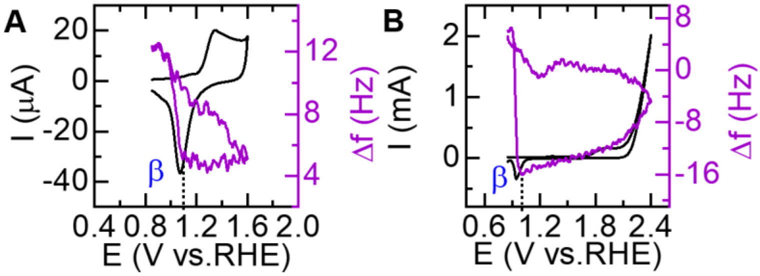

Fig. S7 Electrochemical quartz crystal microbalance measurement with a gold work electrode at 50 mV/s in 0.1 M NaOH. The potential range set is: **(A)** 0.7–1.6 V; **(B)** 0.7–2.4 V vs. RHE. The dash line shows the onset potential of mass loss ($E_ψ$) which reflect the potential in which the QCM signal starts to increase, i.e. mass loss, in the scanning process of a CV.

In an alkaline solution (Fig. 3D), $E_β$ is fixed at 1.1 V providing that E_+ is set lower than 1.7 V. $E_ψ$ was found at 1.13 V unless E_+ is set higher than 2 V. Under these conditions $E_β$ and $E_ψ$ will shift simultaneously with a constant potential difference of $E_{\psi} - E_{\beta} = 0.04\, V$.

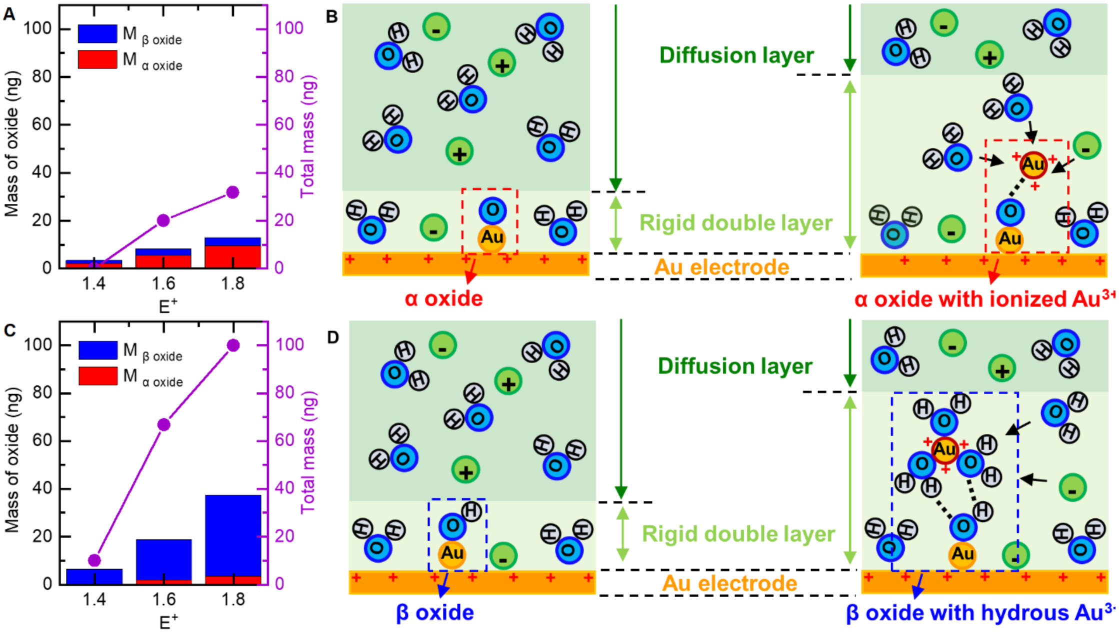

Fig. S8 Mass changes occurring during the formation of α and β oxide as a function of E_+ in 0.1 M $HClO_4$ (A) and 0.1 M $NaClO_4$ (C), and Illustrations of the proposed rigid double layer detected by EQCM at acidic (B) and neutral (D) conditions. The mass changes were calculated from the overall charge transferred during the gold oxidation (red and blue), and obtained from the frequency change detected by the microbalance (purple).The ratio of formed α and β oxide is calculated by the integrated charge of their reduction peaks. The total mass detected by the QCM was calculated from the frequency response by the Sauerbrey equation: $-\Delta f = C_f \cdot \Delta m$, for which a C_f has been determined previously as $8.54*10^7$ Hz/g/cm^2.(*37*)

The quartz crystal microbalance is a very sensitive device that can detect mass changes occurring on the electrode surface during an electrochemical reaction in the order of ng/cm^2. Not only mass changes occurring directly at the electrode surface are detected, but also due to changes occurring in the rigid part of the double layer.(*30-32*) Gold Au^{3+} ions play a massive role in the formation of a rigid double layer structure. Fig. S8A shows how the mass of the electrode changes upon formation of the gold oxide layer as a function of E_+ in 0.1 M $HClO_4$. When E_+ is set at 1.4 V, no mass changes are observed yet by the microbalance, even though α and β oxides have already been formed. This may be related to the process of place exchange between Au and O/OH from adsorption layer at the initial oxide formation process,(*11*) where no new O/OH is fixed from bulk solution into oxide. However, when E_+ is set above 1.5 V, at which Au^{3+} cations are formed and bind onto the surface of α oxide, the total mass detected by the EQCM exceeds the amount of mass that one would expect solely by oxide removal. For this one can simply compare the mass changes expected from formation of Au_2O_3 and $Au(OH)_3$ from the charge, with the mass changes detected by EQCM. Because the EQCM can also detect mass changes into the rigid double layer,(*32, 49*) the extra mass detected by EQCM reflects that more molecules enter the rigid double layer structure from the diffusion layer. The Au^{3+} cations bound to α oxide are expected to bind more water molecules and electrolyte ions, and hold these tightly to the electrode interface resulting in these relatively large mass changes to occur. The proposed mechanism wherein this mass change occurs in an acidic solution is shown in fig. S8B.

Also in a neutral environment, the mass change detected by EQCM is significantly larger than one would expect by solely forming the oxide layer when E_+ is higher than 1.4 V. In this case the major mass changes are related to removal of β oxide rather than α oxide, as shown in fig. S8C. With increase of E_+ in 0.1 M $NaClO_4$, the Au^{3+} produced would form hydrous Au^{3+} and bind to β oxide via a hydrogen bonding network. We observed that changes in computed and detected mass changes are significantly larger at neutral conditions. That indicates that Au^{3+} ions bound to β oxide has a stronger ability to bind molecule tightly in a neutral solution than Au^{3+} ions bound to α oxide in an acidic solution. A cartoon that illustrates how these large mass changes occur in a neutral solution is shown in fig. S8D.

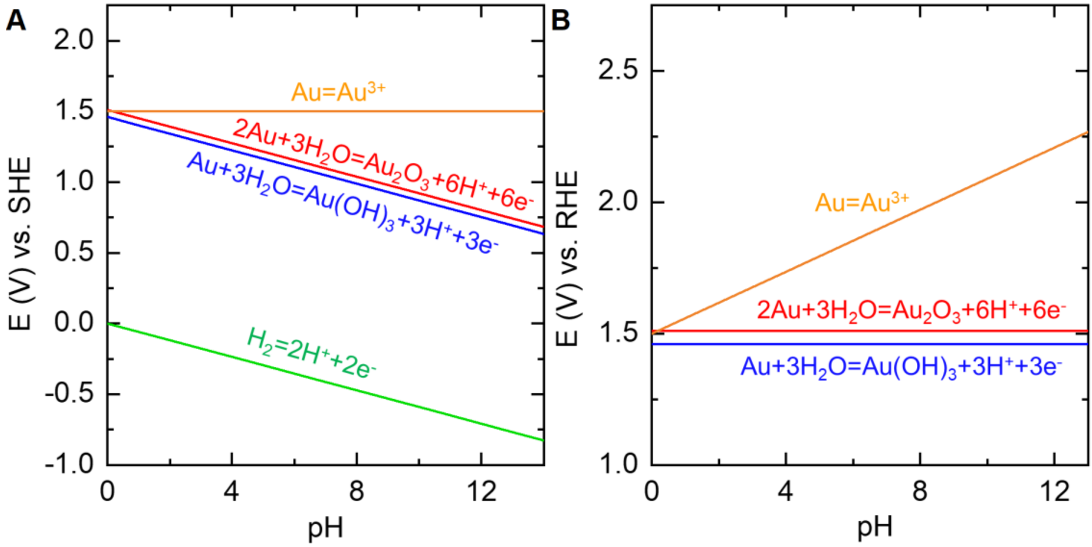

Fig. S9 (**A**)The Pourbaix diagram of gold oxidation and hydrogen oxidation on the SHE scale.(**B**) The E–pH diagram of gold oxidation on the RHE scale.

The initial stages of gold oxidation are associated with sequential formation of sub–lattices of OH or O.(*11*) Pourbaix diagrams of gold (fig. S9A) typically show two stable forms of gold oxide, i.e. Auric oxide ($2Au + 3H_2O \rightarrow Au_2O_3 + 6H^+ + 6e^-$) and Auric hydroxide ($Au + 3H_2O \rightarrow Au(OH)_3 + 3H^+ + 3e^-$).(*44*) When the number of electrons and protons are equal in a Nernst equation, the E–vs–pH plots in a Pourbaix diagram should have an identical slope ($-0.059\ V/pH$ at 25 °C), such as a reversible hydrogen reaction ($2H^+ + 2e^- \rightleftharpoons H_2$) and an ideal metal oxide reduction ($M_2O_x + 2xH^+ + 2xe^- \rightarrow 2M + xH_2O$), as shown in fig. S9A. The oxide reduction potential therefore should occur at a fixed potential independent of pH in a cyclic voltammetry (CV), when the reversible hydrogen electrode (RHE) is used as a reference potential, as shown in fig. S9B.

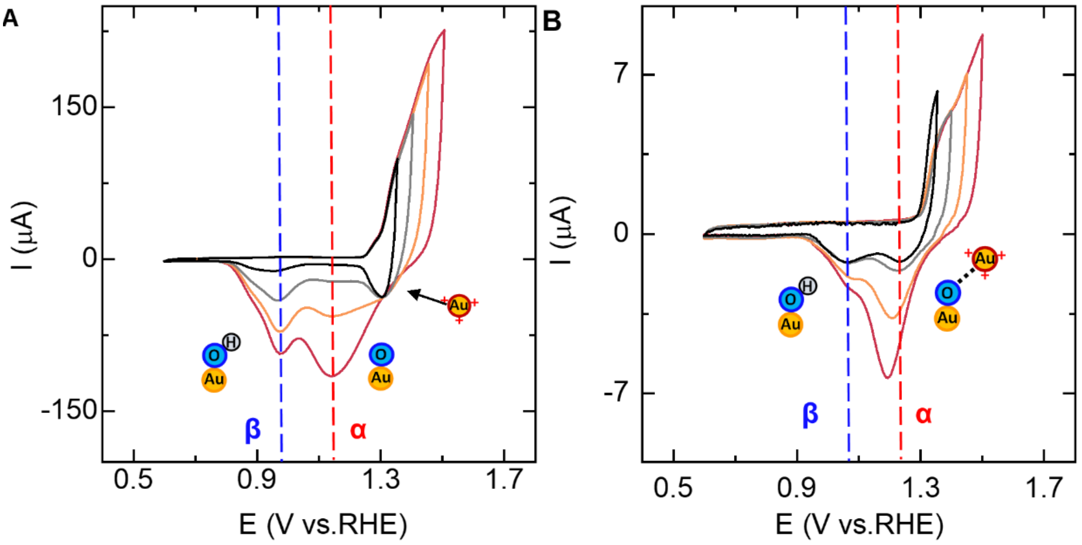

Fig. S10 Cyclic voltammograms of gold at 10 V/s **(A)** and 50 mV/s **(B)** in 0.1M HClO4.

The negative shift of the α peak is caused by the formation of ionic bonds of $Au_2O_3 \cdots Au^{3+}$ that stabilize Au_2O_3. When the scan rate increases from 50 mV/s to 10 V/s, the non–Nernstian behavior will disappear and instead a reversible reduction peak appears at 1.31 V assigned to the reduction of free Au^{3+} (A, black line). Apparently it takes time for Au^{3+} to form ionic bonds with the gold surface. Reversible reduction of free Au^{3+} also appears in cyclic voltammetry experiments at high temperatures (365 K) and high (1 M) concentrations of $HClO_4$.(*35*)

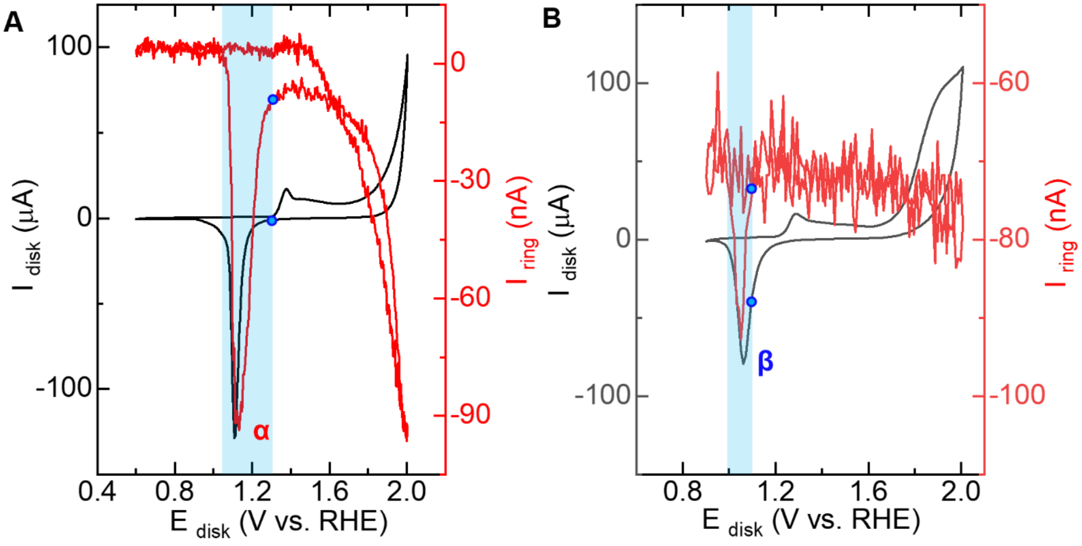

Fig. S11 Rotating ring–disk electrode measurements of gold in 0.1 M $HClO_4$ **(A)** and 0.1 M NaOH **(B)**. $Q_{Au^{3+}}$ is 220 and 24 nC in 0.1 M $HClO_4$ and NaOH, respectively. The blue dot represents the onset potential of Au^{3+}release from the disk, and the onset potential for the detection of released Au^{3+} by its reduction on the ring. The light blue window is the potential region of Au^{3+}release during the gold oxide reduction process.

The onset of Au^{3+} release from α oxide was found to occur simultaneous with the onset of the α peak, and the maximum value observed for Au^{3+} release appears in the first half of the α peak. In contrast, the onset of Au^{3+} release related to reduction of β oxide was observed at a more negative potential which is closer to the peak potential of the β oxide reduction reaction. The maximum value of Au^{3+} release appears during the second half of the β peak.

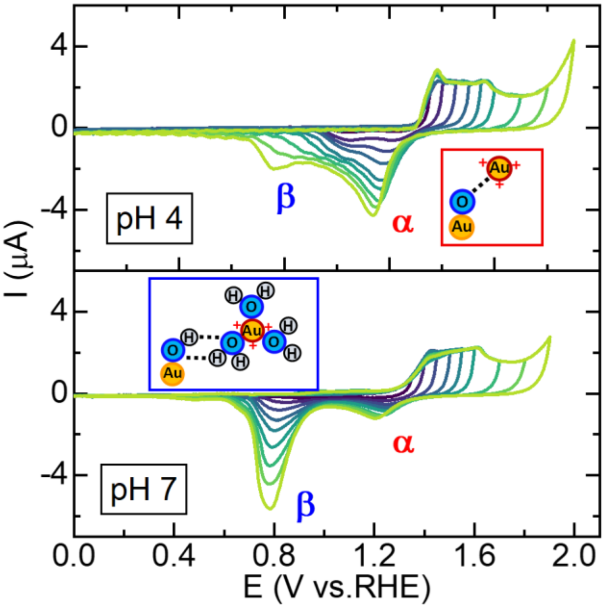

Fig. S12 Cyclic voltammograms in pH 4 and pH 7 at 50 mV/s with varying E_+. The red box shows the proposed α oxide structure leading to non-Nernstian behavior where ionic Au^{3+} binding occurs on α oxide (Au_2O_3). Theblue box shows the proposed β oxide structure leading to non-Nernstian behavior where hydrous Au^{3+} binding occurs on β oxide ($Au(OH)_3$).

Figure S12 reveals the competition between ionized Au^{3+} and hydrous Au^{3+} as a function of pH at mild pH conditions. The non–Nernstian shifts of the α peak and β peaks are caused by Au^{3+} binding to α oxide (see red box) and hydrous Au^{3+} binding to β oxide (see blue box), respectively. We have observed a small negative shift of the β peak and a clear negative shift of the α peak in a mild acidic solution (pH 4), which implies Au^{3+} prefers binding to α oxide in the form of ionized Au^{3+} over binding to β oxide in the form of hydrous Au^{3+}. When the pH of the solution increases to 7, we can observe the β peak with a clear negative shift and a much smaller negative shift of the α peak. This indicates that more stable hydration shells of Au^{3+} have formed on β oxide while less ionized Au^{3+} has appeared on α oxide. These differences of the α and β peak at pH 4 and 7 imply the existence of a competition between the ionized Au^{3+} and hydrous Au^{3+} states within these gold oxides, which is controlled by the concentration of H^+.

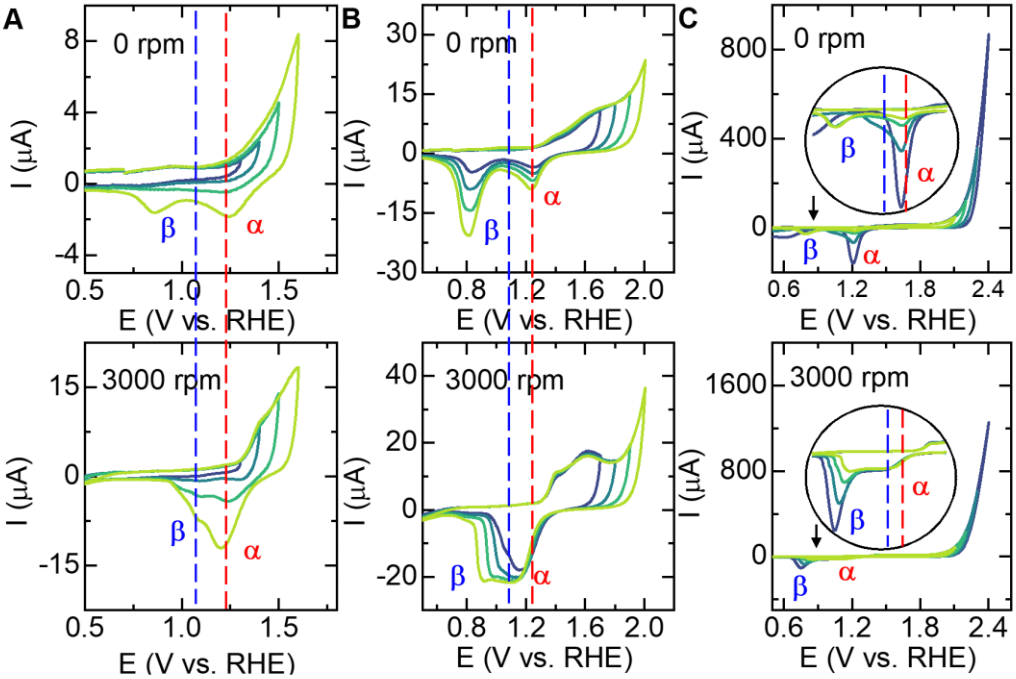

Fig. S13 Cyclic voltammograms in 0.1 M $NaClO_4$ at 50 mV/s under 0 (upper part) and 3000 (lower part) rpm. E^+ is changing from (**A**) 1.3 to 1.6 V; (**B**) 1.7–2 V; (**C**) 2.1–2.4 V. The red and blue dash lines represent the reduction peak potential of initial formation stage of α and β oxide, respectively.

The non–Nernstian behavior is caused by ionic interactions of ionized Au^{3+} on α oxide and hydrogen bonding interaction of hydrous Au^{3+} on β oxide. These two non-covalent interaction are weak. fig. S13A shows that the non–Nernstian behavior of the α and β peaks disappears at 3000 rpm when E_+ is lower than 1.6 V, indicating that the two non-covalent interactions are readily broken when a sufficiently high rotation rate is applied. Upon further increasing E_+ from 1.6 to 2 V (fig. S13B), the β peak shifts to a more negative potential even at rotation rates of 3000 rpm while the α peak appears to be less affected. That indicates that part of the hydrous Au^{3+} cannot escape from the oxide layer. If E_+ is further increased from 2 to 2.4 V (fig. S13C), and under conditions where lots of Au^{3+} are rapidly produced, the β peak disappears under non-rotating conditions while a large α peak can be observed. However the β peak increases quickly upon rotation, while the peak position of the α peak does not change at 3000 rpm. This reveals that a structure changes occur from ionic Au^{3+} to hydrous Au^{3+} upon increase of the high rotation rate. This is most likely due to a more efficient replenishment of water, and removal of H^+ at higher rotation rates.

The phenomenon above is also observed when the electrolyte is changed from $NaClO_4$ to Na_2SO_4.(see fig. S14) This reflects that these observations are independent of the electrolyte.

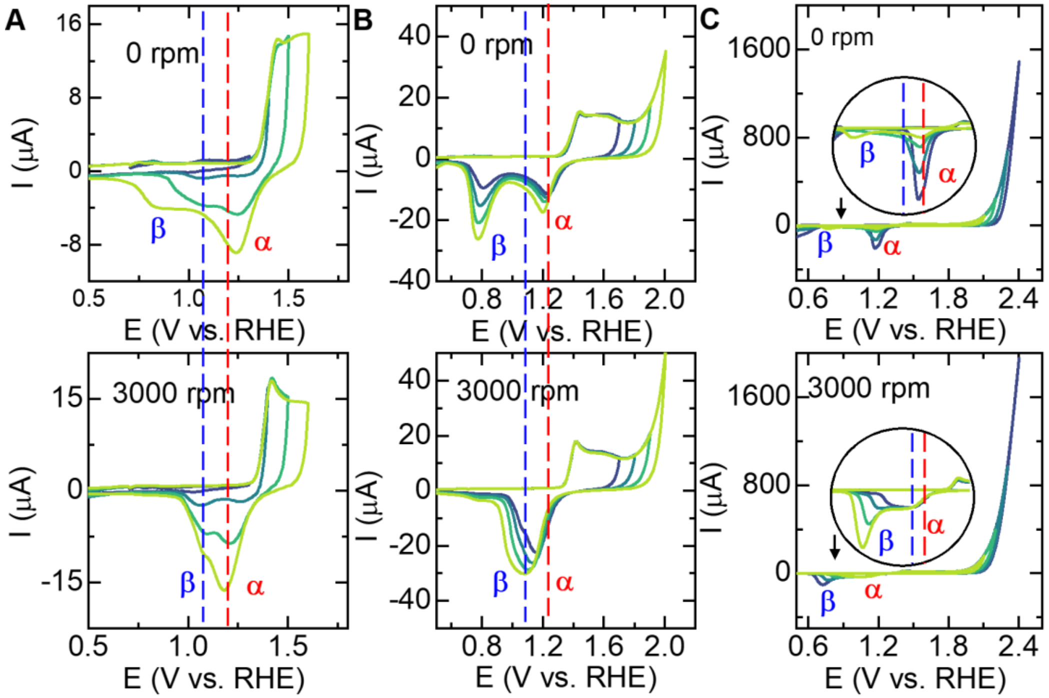

Fig. S14 Cyclic voltammograms in 0.1 M Na_2SO_4 at 50 mV/s under 0 (upper part) and 3000 (lower part) rpm. E^+ is changing from (**A**) 1.3 to 1.6 V; (**B**) 1.7–2 V; (**C**) 2.1–2.4 V. The red and blue dash lines represent the reduction peak potential of initial formation stage of α and β oxide, respectively.

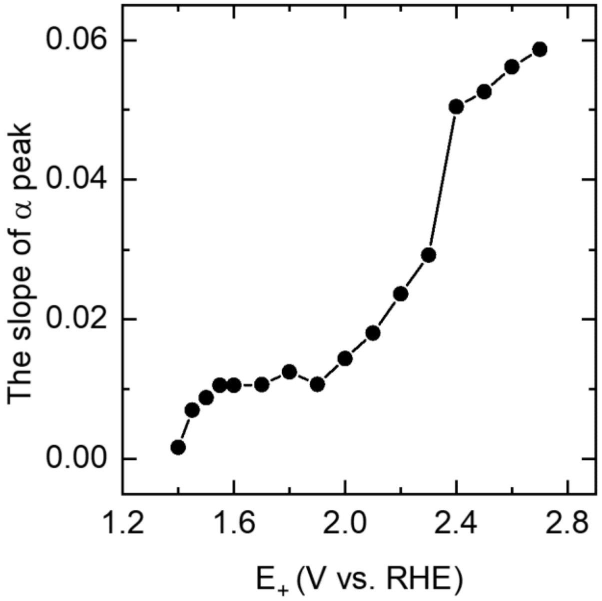

Fig. S15 The slope of the the E_α–vs–pH plots as a function of E_+ obtained from cyclic voltammetry experiments on gold (calculation from the slope in Fig. 1B)

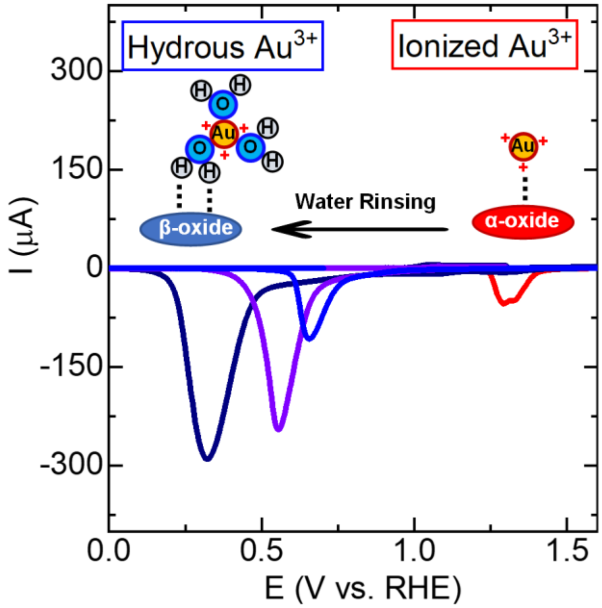

Fig. S16 The effect of Milli-Q water rinsing to position of the α and β reduction peaks of an oxidized gold at 50 mV/s in 0.1 M Na_2SO_4. The red line shows the α reduction peak of oxidized gold without rinsing; the other lines represent the β the reduction peak of oxidized gold after MilliQ water rinsing**.** The total oxidation cycles is 2 cycles (red line), 1 cycles(blue line), 3 cycles (purple line), 5 cycles (dark blue line) in the oxidative region (1.3-2 V), respectively.

In order to further reveal the role of water replenishment to ionized Au^{3+} and hydrous Au^{3+}, we investigated the effect of rinsing with Milli-Q water on the peak potential of the oxide reduction reaction. In this experiment, the gold electrode was first scanned in the oxidative region (1.3–2 V) to form gold oxide in 0.1 M Na_2SO_4. The overall oxidation time was controlled by setting different oxidation cycles in the range of 1.3-2 V. In an control experiment wherein no rinsing occurs (red line), the oxidized gold electrode is directly reduced to obtain the α reduction peak by simple scanning negatively after formation of the oxide in the positive scan. For the other experiments the oxide was produced in the same manner, by oxidation of the gold electrode by scanning positively in the cyclic voltammogram from 1.3-2 V. The electrodes were removed from the solution and rinsed with MilliQ water by a spray bottle for 30 seconds. After rinsing the electrodes were put in a fresh 0.1 M $NaClO_4$ solution to record the peak potential of the oxide reduction reaction. Our experiment shows that the gold oxide reduction peak obtained in an experiment without rinsing by MilliQ water appears at the reduction potential expected for ionized Au^{3+} (1.29 V), while those that were rinsed with MilliQ water appear at the reduction potential of hydrous Au^{3+} (0.32-0.66 V).

Table S1 The total number of Au^{3+} (x) in an Au_2O_3 reduction process based on the slope of α peak in fig. S15

E_+	1.4	1.45	1.5	1.55	1.6	1.7	1.8	1.9	2	2.1	2.2	2.3	2.4	2.5	2.6
x	0.1	0.3	0.3	0.4	0.4	0.4	0.5	0.4	0.6	0.9	0.9	0.9	0.9	0.9	0.9
y	0	0	0	0	0	0	0	0	0	0	yes	yes	yes	yes	yes

Note: x is the number of Au^{3+} in the forms of ionic bonds ($Au_2O_3 \cdots xAu^{3+}$) in the Au_2O_3 reduction process; y shows whether free Au^{3+} exists in the diffusion layer as a result of the saturation of the α oxide with Au^{3+}.

Forms of Electric Charge

复杂背后的本质是简单。

The essence behind complexity is simplicity.

III

Supporting Information for Chapter 4

The PDF file includes:

- Materials and Methods
- Supplementary Text
- Figs. S1 to S13

Materials and Methods

General.

All glassware used in the experiments underwent a thorough cleaning process to remove impurities. This involved submerging the glassware in an aqueous solution containing 0.5 M H_2SO_4 and 6.3 mM $KMnO_4$ overnight. The glassware was then rinsed once with MilliQ water (water with a resistivity of 18.2 MΩ cm). was used to rinse all glassware one time. Next, a mixture of diluted H_2SO_4 and H_2O_2 was added to the glassware in a beaker. This mixture was left for 30 minutes to eliminate excess $KMnO_4$ residue. The glassware underwent five rinses and three rounds of boiling in MilliQ water. Before each electrochemical experiment, the glassware was boiled once more in MilliQ water. Alumina suspensions with particle sizes of 1.0, 0.3, and 0.05 µm were sourced from Buehler. The electrolyte solutions were prepared with Suprapur® reagents from Merck and MilliQ water. pH measurements were carried out using a Hanna Instruments HI 4222 pH meter, calibrated using IUPAC standard buffers.

Electrochemical measurements.

The electrochemical measurements were conducted with approximately 25 °C using Autolab PGSTAT 12, 204 and 128N potentiostats, along with Autolab NOVA software. These measurements were performed in conventional single compartment three–electrode glass cells. The working electrode was a PEEK encapsulated gold electrode with an area of 0.0314 cm^2 (Metrohm). The counter electrode was a gold wire, and a reversible hydrogen electrode (RHE) served as the reference electrodePrior to each measurement, the working electrode was manually polished for 2 minutes using alumina suspensions of decreasing particle size, followed by sonication in MilliQ water for 10 minutes. The counter electrode's gold wire was flame annealed and rinsed with MilliQ water. The reference electrode (RHE) was constructed using a Pt wire connected via a Luggin capillary and continuously bubbled with H_2 gas during the measurements.

In the absence of particular indications, the pH values spanning from 1 to 13 were achieved by mixing perchloric acids, sodium hydroxide, and sodium perchlorate to maintain a consistent ionic strength for different pH levels. Different types or concentrations of anions were used for solution variations. All electrochemical experiments were conducted under either saturated argon (Ar) or saturated oxygen (O_2) conditions. For the Ar experiments, dissolved O_2 was removed from the solution by bubbling argon for at least 30 minutes, and argon was maintained above the solution throughout the experiments. Similarly, for O_2 experiments, the solution was bubbled with pure O_2 for at least 30 minutes, with O_2 continuously flowing above the solution.

Electrochemical quartz crystal microbalance (EQCM)

EQCM experiments were carried out using an Autolab PGSTAT 128N potentiostat and a 5 mL Autolab EQCM cell. A gold–coated quartz crystal EQCM electrode with an area of 0.35 cm^2 and a gold layer thickness of 200 nm was used as the working electrode. A coiled gold wire served as the counter electrode. The custom–made electrochemical cell, constructed from PEEK material, had a volume of 5 mL. An RHE Luggin setup was employed as the reference electrode.(*33*)

EQCM experiments were conducted using an Autolab PGSTAT 128N potentiostat and a 5 mL Autolab EQCM cell. An Autolab gold coated quartz crystal EQCM electrode (A = 0.35 cm^2, gold layer thickness = 200 nm, the fundamental frequency of quartz crystal is 6 MHz) was used as the working electrode and a coiled gold wire was used as the counter electrode. The custom made electrochemical cell consisted of PEEK material and had a volume of 5 mL. An RHE Luggin setup was used as the reference electrode.(*33*)

Supplementary Text

S1 Understanding redox processes of X and Y: pH and electrolyte influence

In order to perform a quantitative comparison of the peak potentials associated with the redox processes X and Y, various parameters were examined in relation to the Pourbaix diagram. Specifically, the oxidation peak potentials (E_{X^+}) and reduction peak potentials (E_{X^-})

of the X redox couple, as well as the corresponding values for the Y redox couple (E_{Y}+) and (E_{Y}−), were plotted against pH (as depicted in Fig. 5B and Fig. 5C). An intriguing observation emerged: E_{X}+ (0.31 V vs. NHE) and E_{X}− (0.19 V vs. NHE) remain constant regardless of pH, as long as pH is below 8. Contrarily, E_{Y}+ and E_{Y}− exhibit a consistent shift of –59 mV/pH on the Pourbaix diagram, but only within the pH range of 8 to 13. This distinction indicates that the X redox process involves electron transfer (ET) exclusively in the pH range of 1 to 8. In contrast, the redox process of Y involves a proton coupled electron transfer (PCET) mechanism.

When the concentration of the $NaClO_4$ electrolyte was varied from 0.1 M to 0.05 M or 0.01 M, a remarkable shift towards more negative potentials was observed for X, correlating with a decreasing electrolyte concentration observed (Fig. 5A, Fig. S5 and Fig. S6). Conversely, Y displayed no shift in potential under these conditions. These findings suggest that the equilibrium potential of X is influenced by electrolyte concentration, while that of Y remains unaffected. Additional cyclic voltammetry (CV) experiments were performed on gold electrodes in both 0.1 M (Fig. S7) and 0.01 M Na_2SO_4 (Fig. S8) solutions under identical experimental conditions. These experiments further validate that the peak potentials of the X and Y redox processes as a function of pH are governed by the expressions $E_X = E_X^0 + 0\ mV/s\ (V\ vs.NHE)$ and $E_Y = E_Y^0 + 0.059\ V/s\ (V\ vs.NHE)$, respectively, regardless of whether ClO_4^{-} or SO_4^{2-} solutions were employed. Notably, it was observed that E_X^0 varied with electrolyte concentration (ranging from 0.01 M to 0.1 M) and the type of anions (ClO_4^{-}, SO_4^{2-}) while E_Y^0 exhibited no such relationship with the electrolyte composition (Fig. S9A and B). This observation strongly implies that the X redox wave should be attributed to anion adsorption/desorption events occurring at the surface. Additionally, the average current of the X redox save (I_X) is maintained at the same value in the 0.1 M and 0.05 M $NaClO_4$ solutions, but appears to decrease slightly in 0.01 M $NaClO_4$ (Fig. S9C). It is worth noting that the shifts in chemisorbed bonds of different anions (NO_3^{-},ClO_4^{-} or SO_4^{2-}) in the potential region where X appears have been directly detected on the Au(111) surface using different in situ spectroscopy techniques (*20, 34, 35*). We therefore assign the X redox equilibrium to the chemical adsorption and desorption of anions on the Au surface.

On the other hand, the Y redox process was attributed to OH^{-} adsorption and desorption, especially in alkaline solutions (*36, 37*). Besides, it was found that I_Y remains independent of electrolyte concentration at pH values below 8, yet becomes sensitive to the overall electrolyte concentration at higher pH values (Fig. S9D). Consistently, the Y redox couple adheres to $E_Y \ = 0.8\,V - 0.059\ V/pH\ \ (V\ vs. NHE)$, remaining unaffected by the electrolyte concentration (Fig. S9B). This insight leads us to attribute the redox event Y to the chemical adsorption and desorption of hydroxide ions on the gold surface.

S2. The E_{ORR} dependence on the O_2 concentration.

In order to investigate the ORR activity, cyclic voltametry (CV) was used to investigate the potential at which the ORR occurs on polycrystalline gold in solutions of different pH. Initially, we manipulated the upper limit of the CV (E_+) to control the ocurrence of the oxygen evolution reaction within Ar–saturated 0.1 M $HClO_4$ (as shown in the top part of Fig. S10A) and 0.1 M NaOH (as illustrated in the top part of Fig. S10B). By setting E_+ above the onset potential of the oxygen evolution reaction ($onset_{OER}$), the ORR peak could be discerned during the negative scan of the CVs.

As we further elevated E_+ to increase the concentration of O_2 at the working electrode, and subsequently scanned the potential in the direction of ORR with both of Ar–saturated 0.1 M $HClO_4$ and 0.1 M NaOH, a noteworthy observation was made. The peak current of the ORR increased, yet the peak potential of the ORR (E_{ORR}) remained consistent. This behavior was observed irrespective of whether the solution was Ar–saturated (the top part of Fig. S10A and B) or O_2–saturated (the bottom part of Fig. S10A and B). Notably, in the O_2–saturated environment, the E_+ value was fixed at 1 V vs. RHE, maintained at a level lower than the potential for gold oxidation. This measure was taken to mitigate any potential interference stemming from gold oxide during the ORR.

The consistency of E_{ORR} under O_2– saturated conditions, as compared to E_{ORR} under Ar–saturated conditions, was confirmed in both 0.1 M $HClO_4$ and 0.1 M NaOH solutions. As a result of its consistency and precision on polycrystalline gold, E_{ORR} was considered to be a useful metric to monitor changes in ORR activity across the entire pH spectrum.

Furthermore, it is crucial to acknowledge that determining the precise onset potential of the ORR ($\text{onset}_{\text{ORR}}$) can be challenging due to its overlap with the potential region where the gold oxide reduction reaction occurs. This overlap is particularly pronounced in neutral and alkaline solutions. For the purposes of this manuscript, the choice was made to rely on E_{ORR} rather than $\text{onset}_{\text{ORR}}$ as the metric to track variations in ORR activity across all pH values.

S3. Surface charge calculation under saturated Ar

During the development of the mathematical model for calculating surface charge at 0.1 M $NaClO_4$, based on the EQCM system, certain definitions and simplifications were employed. These definitions are crucial for a comprehensive understanding of the calculations:

a) The electrolyte is treated as an ideal solution, maintaining a total concentration of 0.1 mol/L by mixing equimolar concentrations of $HClO_4$, $NaClO_4$, NaOH.

b) The potential region of zero charge (PRZC) marks the potential range where the frequency response recorded by EQCM remains minimum and undergoes no change. Onset_{C^-} signifies the point where $-\Delta f$ begins to increase upon an decreasing applied potential. Conversely, onset_{C^+} marks another transition point, where $-\Delta f$ begins to increase with an increasing applied potential.

c) When the applied potential surpasses the onset_{C^+} in a CV conducted under saturated Ar, the gold surface accumulates an excess of positive charge, leading to the attraction of anions from the solution through electrostatic interactions. This potential range is referred to as the C^+ zone.

d) Conversely, when the applied potential falls below the onset_{C^-}, the gold surface carries an excess negative charge, resulting in the attraction of cations from the solution through electrostatic interactions. This potential range is referred to as the C^- zone.

e) The excess charge calculation solely encompasses the excess charge in the C^+ and C^- zones, while disregarding the potential influence of cation adsorption, hydrogen adsorption and evolution at more negative potentials, oxide formation, and oxygen evolution at more positive potentials.

The range of PRZC under saturated Ar is defined based on the EQCM response. In addition:

When the pH is below 8, the X redox couple is observed in the PRZC.

When pH is 8 or higher, the Y redox couple is observed in the PRZC.

The mathematical model's development involved three key steps:

(1) The differential capacitance C under Ar in the electrical double layer (EDL) potential region:

The differential capacitance (C) in the EDL potential region can be determined using the equation:

$$C = \frac{I^{+} - I^{-}}{2 \times \nu \times A}.$$

where I^{+} and I^{-} represent the currents during positive and negative CV scans, ν is the scan rate (50 mV/s), and A is the electrode surface area (0.0314 cm^2). When the electrolyte concentration is 0.1 mol/L, C is calculated to be 18 $\mu F/cm^2$, as shown in Fig. 8A.

(2) The net Faradaic charge distribution of the redox couple in the PRZC

To quantify the chemical adsorption and desorption processes of a surface redox couple at a specific potential, the integrated oxidation and reduction charges are determined. The net integrated charge at that potential is the sum of the integrated oxidation and reduction charges as shown in Fig. S12. Mathematically:

Integrated oxidation charge ($\Delta Q_{X^{+}}$) during positive CV scan: $\Delta Q_{X^{+}} = \frac{\int I^{+} \cdot dU}{\nu \times A}$;

Integrated reduction charge ($\Delta Q_{X^{-}}$) during negative CV scan: $\Delta Q_{X^{-}} = -\frac{\int I^{-} \cdot dU}{\nu \times A}$;

Net integrated charge (ΔQ) at a specific potential: $\Delta Q = \Delta Q_{X^{+}} + \Delta Q_{X^{-}}$.

The calculations for the net charge of the Y redox reaction mirror those for the X redox reaction.

Where I^{+} is the current at a positive scan of a CV and I^{-} is the current at a negative scan of a CV; ν is the scan rate (50 mV/s); A is the electrode surface area (0.0314 cm^2); $\int I^{+} \cdot dU$ is the integrated area of CV at the positive scan; $\int I^{-} \cdot dU$ is the integrated area of a CV at the negative scan.

(3) The excess charge distribution in the EDL potential region.

Excess charge is calculated in the C$^+$ and C$^-$ zones:

Positive excess charge in C$^+$ zone: $\Delta Q^{+} = \frac{C\times(E-\text{onset}_{C+})}{A}$;

Negative excess charge in C$^-$ zone: $\Delta Q^{-} = \frac{C\times(E-\text{onset}_{C-})}{A}$;

Here, C is the capacitance (18 μF/cm^2), E represents a specific potential point in the CV, and A signifies the electrode surface area (0.0314 cm^2).

S4. Surface excess charge calculation under saturated O_2

Under O_2–saturated solutions, the oxygen reduction reaction (ORR) brings about two prominent effects on the electrical double layer (EDL) structure in comparison to conditions under saturated Ar:

(1) A changes in the potential regions for the PRZC , C$^-$ and C$^+$ zone:

A surface redox couple arises within the PRZC that is pinpointed by a minimum $-\Delta f$ in EQCM experiments. Under Ar conditions, anion redox reactions (X potential region) occur within the PRZC in the pH range of 1 to 8. However, redox reactions involving hydroxide (Y potential region) emerge within the PRZC when the pH exceeds 8. When the pH increases, the potential of the X redox wave shifts positively towards the potential of the Y redox wave in a cyclic voltammogram (CV). For pH values higher than 8, the X peak changes from an electron transfer (ET) process (pH 1–8) to a proton coupled electron transfer (PCET) process similar to the Y redox reaction.

Since the X and Y regions are not discernible under O_2 conditions, it is crucial to emphasize that the characterization of the X and Y regions within this manuscript specifically pertains to their presence under Ar. It is worth highlighting that when the pH remains below 8, the width of the PRZC narrows causing the onset c^{+} to shift in a negative potential. Conversely, as the pH surpasses 8, the PRZC widens with a negative potential shift of the onset c^{-}.

To conclude, when the pH remains below 8, the PRZC observed in O_2–saturated solutions aligns with the onset c^{-} observed in Ar–saturated solutions. Conversely, when the pH reaches 8 or higher, the PRZC observed in O_2–saturated solutions corresponds to the combined representation of both the X and Y regions observed under Ar–saturated solutions.

(2) A diminished capacitance in the C^{-} zone and an unaffected capacitance in the C^{+} zone:

The ORR leads to electron consumption on the gold surface and decreasing negative excess charge within the C^{-} zone. Since the $-\Delta f$ increase correlates with the surface excess charge, a ratio of $-\Delta f$ change under Ar and O_2 conditions can be established (depicted in Fig. S13). This ratio serves as a corrective coefficient (K) for the capacitance under saturated O_2, expressed as $K=\frac{(\frac{-\Delta f}{\Delta E})_{O_2}}{(\frac{-\Delta f}{\Delta E})_{Ar}}=\frac{C_{O_2}}{C_{Ar}}$, where $(\frac{-\Delta f}{\Delta E})_{O_2}$ and $(\frac{-\Delta f}{\Delta E})_{Ar}$ signify the frequency change slope at specific potentials under saturated Ar and O_2, respectively. This corrective coefficient allows the determination of capacitance under saturated O_2, denoted as as $C_{O_2}=K\times C_{Ar}$. Here, C_{O_2} represents the capacitance under saturated O_2, K is the corrective coefficient, and C_{Ar} is the capacitance under saturated Ar.

Excess charge in the C^{-} potential region:

As K exhibits variation with changes in E wihin the C^{-} zone, expressed by the equation K=0.18– 0.24*E (Fig. S13B), we can calculate ΔQ as follows: $\Delta Q=K\times\frac{C\times(E-\mathrm{onset}_{C^{-}})}{A}$;

Excess charge (ΔQ) in the C^{+} potential region:

Since K remains at 0.8 whinin the C$^+$ zone, with $C_{O_2} = 0.8 \times C_{Ar}$ (Fig. S13C). we calculate ΔQ as follows: $\Delta Q = \frac{C_{O_2} \times \Delta E}{A} = \frac{0.8\, C_{Ar} \times (E - \text{onset}_{C^+})}{A}$;

Here, K represents the corrective coefficient for capacitance under O_2–saturated conditions. This comprehensive approach allows the accurate calculation of surface excess charge under saturated O_2, considering the distinctive effects introduced by ORR and changes in EDL structure.

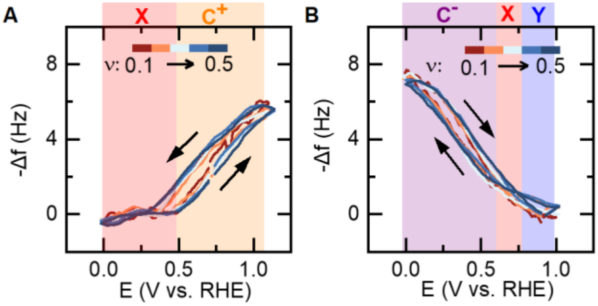

Fig. S1 Dependence of frequency change on the scan rate (v) in 0.1 M $HClO_4$ (A) or NaOH (B). The X and Y regions indicate the potential ranges in which the X and Y redox couples can be identified in a CV, respectively. C$^+$ signifies the potential region of positive excess charge, while C$^-$ represents the potential region of negative excess charge.

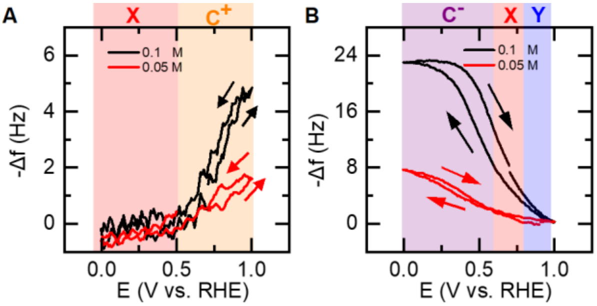

Fig. S2 Dependence of the Frequency change on the electrolyte concentration. (A) $HClO_4$ and (B) NaOH. The X and Y regions correspond to the potential regions in which the X and Y redox couples can be identified in a CV, respectively. C$^+$ indicates the potential region of positive excess charge, while C$^-$ represents the potential region of negative excess charge. Black lines and red lines correspond to measuring concentrations of electrolyte at 0.1 M and 0.05 M, respectively.

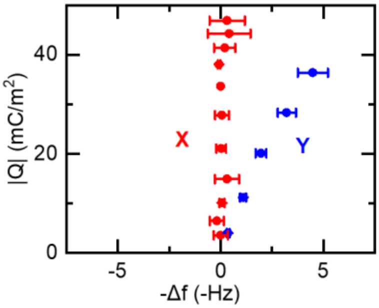

Fig. S3 Comparison of the frequency response observed by EQCM and the absolute integrated charge of the redox peaks in 0.1 M $HClO_4$ (X) and 0.1 M NaOH (Y).

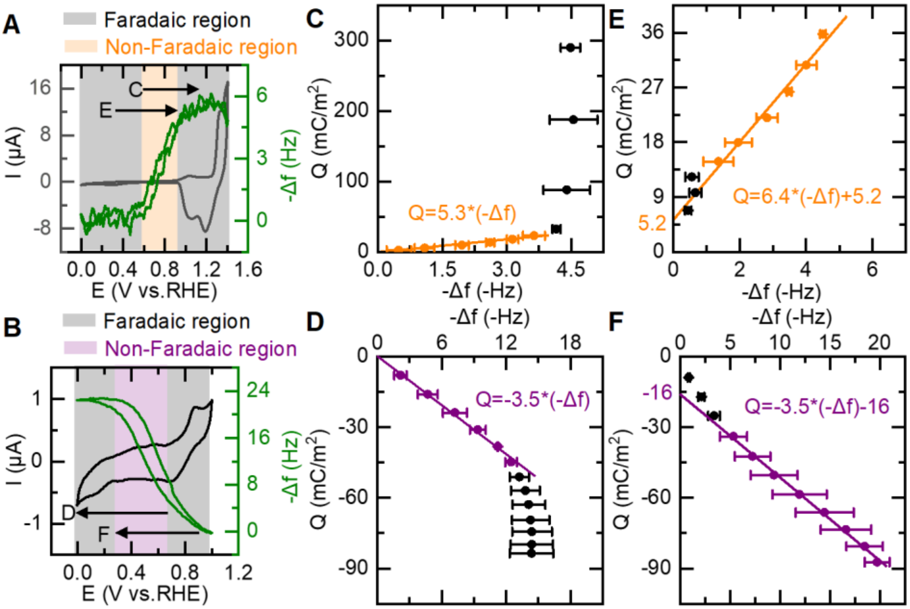

Fig. S4 EQCM measurements in different electrolyte solutions. (A) EQCM measurements conducted in 0.1 M $HClO_4$. The arrows (C, E) indicate the potential windows for charge integration (Fig. S4C and E), respectively. **(B)** EQCM measurements conducted in 0.1 M NaOH. The arrows (D, F) indicate the potential windows for charge integration (Fig. S4 D and F). **(C)** Relationship between the integrated charge of a CV (ΔQ) and the corresponding negative frequency change (– Δf) when the applied potential transitions from the non– Faradaic region (orange part) to the Faradaic region (black part) in 0.1 M $HClO_4$. The arrow C in Fig. S4A indicates the start point and end point of the charge integration from which the relationship between ΔQ and and –Δf in Fig. S4C is determined. **(D)** Relationship between the integrated charge of a CV (ΔQ) and the corresponding negative frequency change (– Δf) when the applied potential transitions from the non– Faradaic region (purple part) to the Faradaic region (black part) in 0.1 NaOH. The arrow D in Fig. S4B indicates the start point and end point of the charge integration from which the relationship between ΔQ and–Δf in Fig. S4D is determined. **(E)** Relationship between the integrated charge of a CV (ΔQ) and the negative frequency change (– Δf) when the applied potential shifts from the Faradaic region (black part) to the non– Faradaic region (orange part) in 0.1 M $HClO_4$. The arrow E in Fig. S4A indicate the start point and end point of the charge integration from which the relationship between ΔQ and and –Δf in Fig. S4E is determined. **(F)** Relationship between the integrated charge of a CV (ΔQ) and the negative frequency change (– Δf) when the applied potential shifts from the Faradaic region (black part) to the non– Faradaic region (purple part) in 0.1 M NaOH. The arrow F in Fig. S4B indicate the start point and end point of the charge integration from which the relationship between ΔQ and–Δf in Fig. S4F is determined.

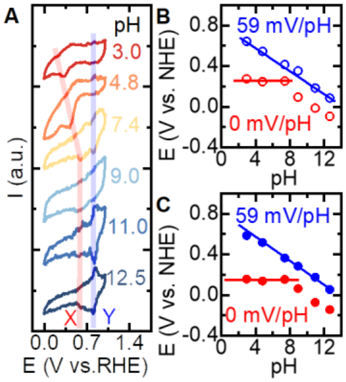

Fig. S5 pH dependence of the X and Y peaks in the electrochemical double layer region. **(A)** CVs of gold in various Ar– saturated pH solutions at a scan rate of 50 mV/s. **(B)** Pourbaix diagram of X^+ (E_{X^+}) and Y^+ (E_{Y^+}) redox peaks in the positive scan of CVs of gold. **(C)** Pourbaix diagram of X^- (E_{X^-}) and Y^- (E_{Y^-}) redox peaks in the negative scan of CVs of gold. The concentration of ClO_4^- is maintained at 0.05 mol/L.

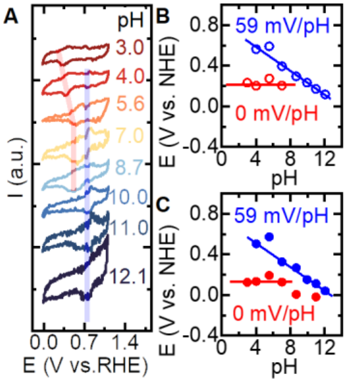

Fig. S6 pH dependence of the X and Y redox peaks in the electrochemical double layer region under diluted conditions. (A) CVs of gold in various Ar– saturated pH solutions at a scan rate of 50 mV/s. **(B)** Pourbaix diagram of X^+ (E_{X^+}) and Y^+ (E_{Y^+}) redox peaks in the positive scan of CVs of gold. **(C)** Pourbaix diagram of X^- (E_{X^-}) and Y^- (E_{Y^-}) redox peaks in the negative scan of CVs of gold. The concentration of ClO_4^- is maintained at 0.01 mol/L.

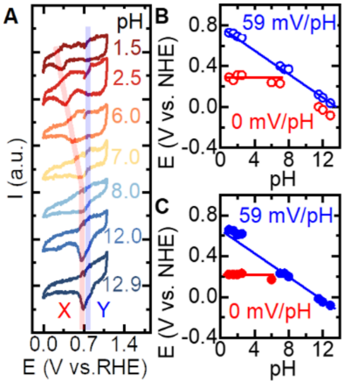

Fig. S7 pH dependence of the X and Y peaks in the electrochemical double layer region in sulfate solutions. (A) CVs of gold in various Ar– saturated pH solutions at a scan rate of 50 mV/s. **(B)** Pourbaix diagram of X^+ (E_{X^+}) and Y^+ (E_{Y^+}) redox peaks in the positive scan of

CVs of gold. **(C)** Pourbaix diagram of X⁻ (E_{X^-}) and Y⁻ (E_{Y^-}) redox peaks in the negative scan of CVs of gold. The concentration of SO_4^{2-} is maintained at 0.1 mol/L.

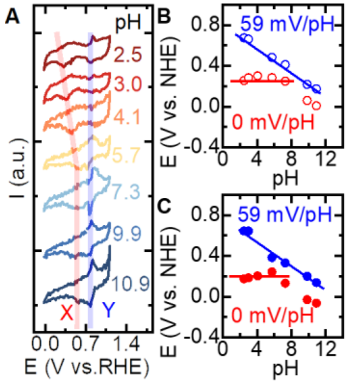

Fig. S8 X and Y redox peaks in the electrochemical double layer region under diluted conditions. (A) CVs of gold in different Ar– saturated pH solutions at a scan rate of 50 mV/s. **(B)** Pourbaix diagram of X⁺ (E_{X^+}) and Y⁺ (E_{Y^+}) redox peaks in the positive scan of CVs of gold. **(C)** Pourbaix diagram of X⁻ (E_{X^-}) and Y⁻ (E_{Y^-}) redox peaks in the negative scan of CVs of gold. The concentration of SO_4^{2-} is maintained at 0.01 mol/L.

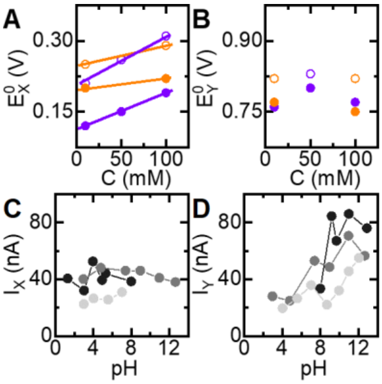

Fig. S9 Effect of electrolyte concentration on the potential and current of X and Y peaks. (A) The $E_{X^+}^0$ (open circle) at the positive scan and $E_{X^-}^0$ (solid circle) at the negative scan of CV in different concentrations of ClO_4^- (violet) and SO_4^{2-} (orange) [$E_X = E_X^0 - 0\ mV/s\ (V\ vs. NHE)$]. **(B)** The $E_{Y^+}^0$ (open circle) at positive scan and $E_{Y^-}^0$ (solid circle) at negative scan in different concentrations of ClO_4^- (violet) and SO_4^{2-} (orange) [$E_Y = E_Y^0 -$

$0.059\ V/s\ (V\ vs. NHE)$]. **(C)** The average peak current I_X ($I_X = \frac{I_{X+} - I_{X-}}{2}$) in the concentration of 0.1 M (black), 0.05 M (dark grey), and 0.01 M (light grey) of ClO_4^-. **(D)**The average peak current I_Y ($I_Y = \frac{I_{Y+} - I_{Y-}}{2}$) in the concentrations of 0.1 M (black), 0.05 M (dark grey), and 0.01 M (light grey) of ClO_4^-.

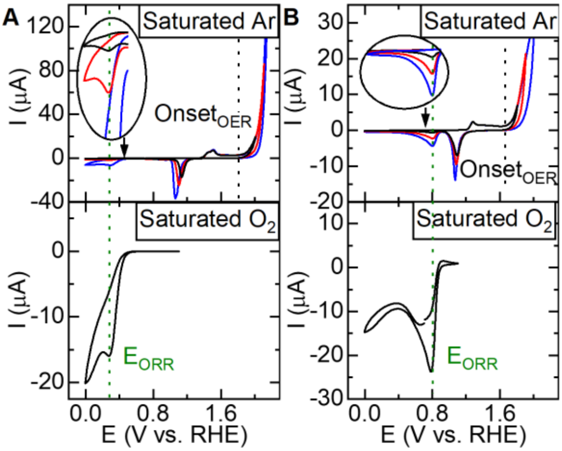

Fig. S10 CVs of gold in Ar–saturated (top) and O_2–saturated (bottom) 0.1 M $HClO_4$ (A) and 0.1 M NaOH (B) at 50 mV/s. Black and olive dotted lines represent the onset potential of the oxygen evolution reaction (Onset$_{OER}$) and the peak potential of the oxygen reduction reaction (E$_{ORR}$), respectively.

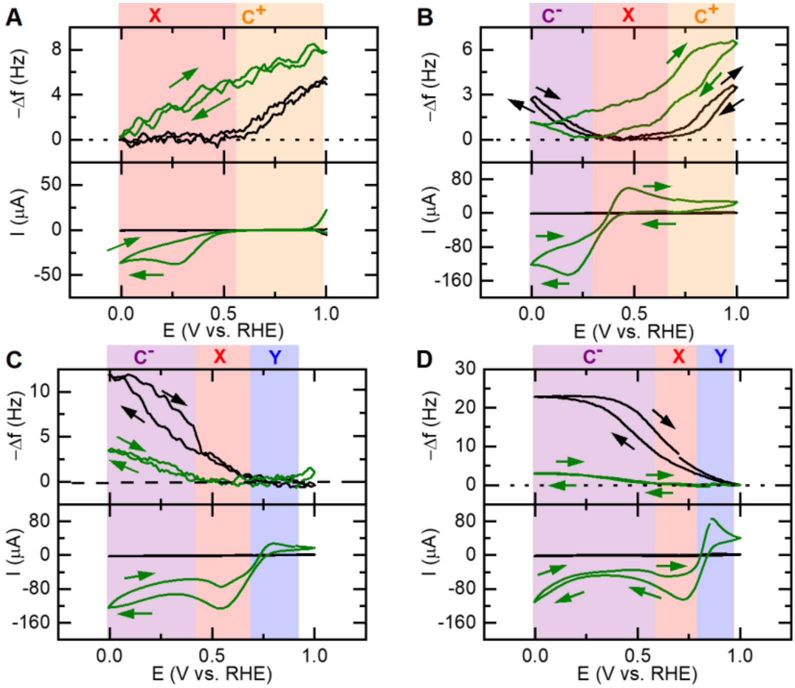

Fig. S11 EQCM measurements in Ar–saturated (black line) and O_2–saturated (green line) solutions at pH solutions. pH 1 **(A)**, pH 4 **(B)**, pH10 **(C)**, pH 13 **(D)**. X and Y regions represent the potential regions in where X and Y redox couples can be detected in a CV under saturated Ar, respectively. C^+ signifies the potential region of positive excess charge, while C^- represents the potential region of negative excess charge.

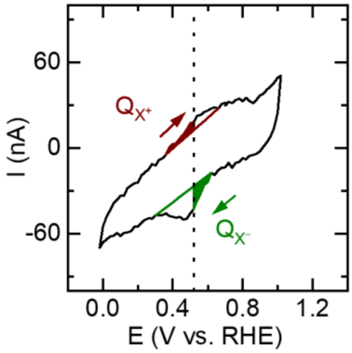

Fig. S12 Intergrated charge of X redox couple in a CV at pH 5 under saturated Ar. Integrated charge of X adsorption at positive scan is $Q_{X^+} = \frac{\int I^+ \cdot dU}{\nu \times A}$, where $\int I^+ \cdot dU$ represents the integral area of X at positive scan (dark red part). Integrated charge of X desorption at the negative scan is $Q_{X^-} = -\frac{\int I^- \cdot dU}{v \times A}$, where $\int I^- \cdot dU$ represents the integral area of X at negative scan (dark green part). v is the scan rate, and A is the surface area of gold electrode.

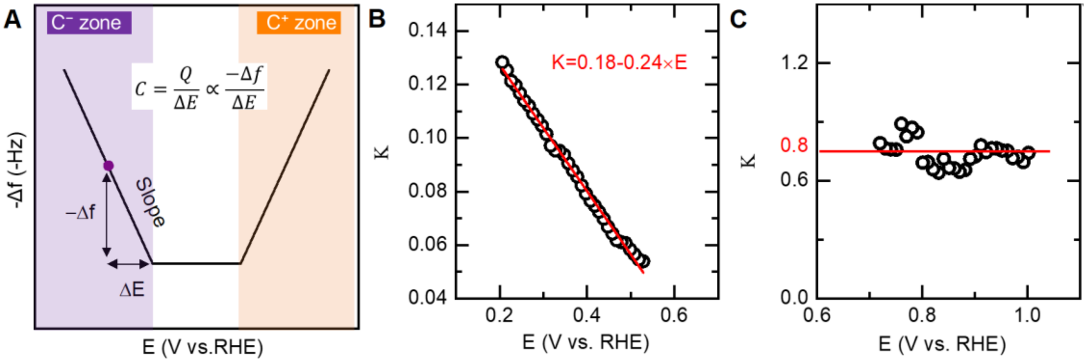

Fig. S13 Corrective coefficient (K) of the capacitance under O₂. (A) Graph that illustrates how the capacitance is calculated at each potential utilizign the frequency response in EQCM. Given that frequency changes in EQCM are directly propotional to surface charge, the slope of these frequency changes is linked to capacitance through the equation $C = \frac{\Delta Q}{\Delta E} \propto \frac{-\Delta f}{\Delta E}$. The corrective coefficient (K) is defined as the ratio of $(\frac{-\Delta f}{\Delta E})_{O_2}$under O_2 to $(\frac{-\Delta f}{\Delta E})_{Ar}$ under Ar at each applied potential (E). This relationship is represented by $K = \frac{(\frac{-\Delta f}{\Delta E})_{O_2}}{(\frac{-\Delta f}{\Delta E})_{Ar}} = \frac{C_{O_2}}{C_{Ar}}$. **(B)** The K of capacitance under O_2 in the C⁻ zone. A linear relationship between K and E is observed in the C⁻ zone, with the equation K=0.18– 0.24× E. This indicates that the capacitance under O_2 is diminished in the C⁻ zone comparing with that under Ar. **(C)** The K of capacitance under O_2 in the C⁺ zone. K is of roughly 0.8 is found indepedent of the potential indicating that the ratio of capacitance under O_2 and capacitance under Ar is constant.